Kim *et al. Energy Mater.* **2025**, *5*, 500097
DOI: 10.20517/energymater.2024.244

Energy Materials

Review

Open Access

Recent advances in Ni-based electrocatalysts for low-energy hydrogen production via alternative pathways to water electrolysis

Minsu Kim[1,#], Sehyun Joung[1,#], Seungjune Lee[1], Heedong Kwon[1], Hyoyoung Lee[1,2,3,4,*]

[1]Department of Chemistry, Sungkyunkwan University (SKKU), Suwon 16419, Republic of Korea.
[2]Institute of Quantum Biophysics, Sungkyunkwan University (SKKU), Suwon 16419, Republic of Korea.
[3]National Institute of Climate and Environment, Sungkyunkwan University (SKKU), Suwon 16419, Republic of Korea.
[4]CO2 to Multicarbon Production Center, Sungkyunkwan University (SKKU), Suwon 16419, Republic of Korea.
[#]Authors contributed equally.

[*]**Correspondence to:** Prof. Hyoyoung Lee, Department of Chemistry, Sungkyunkwan University (SKKU), 2066, Seoburo, Jangan-gu, Suwon 16419, Republic of Korea. E-mail: hyoyoung@skku.edu

How to cite this article: Kim, M.; Joung, S.; Lee, S.; Kwon, H.; Lee, H. Recent advances in Ni-based electrocatalysts for low-energy hydrogen production via alternative pathways to water electrolysis. *Energy Mater.* **2025**, *5*, 500097. https://dx.doi.org/10.20517/energymater.2024.244

Received: 31 Oct 2024 **First Decision:** 3 Dec 2024 **Revised:** 25 Dec 2024 **Accepted:** 30 Dec 2024 **Published:** 7 May 2025

Academic Editors: Yuhui Chen, Xili Tong **Copy Editor:** Ping Zhang **Production Editor:** Ping Zhang

Abstract

Energy-efficient water electrolysis is one of the most promising techniques for generating green hydrogen as a carbon-free energy source. As a half-reaction of water splitting, the oxygen evolution reaction is kinetically sluggish, leading to large thermodynamic potential gaps compared to the hydrogen evolution reaction. In terms of cost-effective hydrogen generation, mitigating this overpotential is a challenging obstacle, but it remains a hurdle to overcome. It is necessary to advance energy-saving hydrogen production by substituting with an oxygen evolution reaction as a thermodynamically favorable anodic reaction. Additionally, depending on the specific small molecules used for the anodic oxidation reaction, it is possible to reduce environmentally harmful substances and produce value-added chemicals. Nickel-based electrocatalysts have received growing attention for their application in electrochemical reactions due to their affordability, versatility in structural tuning, and ability to function as active sites for bond formation and cleavage. The purpose of this paper is to probe how the morphology, structure, and composition of these catalysts affect the electrocatalyst performance for small molecule oxidation. Explaining these relationships can accelerate the development of sustainable hydrogen production techniques by identifying the design principles of high-performance nickel-based electrocatalysts.

Keywords: Energy-saving hydrogen production, electrocatalyst, Ni-based catalyst, urea oxidation, hydrazine oxidation, ammonia oxidation, oxidation of small molecules

INTRODUCTION

It is widely acknowledged that the use of fossil fuels should be reduced due to environmental pollution and global warming problems[1]. Sustainable energy conversion and production technologies are being actively developed to reduce reliance on fossil fuels[2]. Hydrogen is one of the most efficient and promising alternatives to replace fossil fuels as a sustainable energy source[3].

Hydrogen has an energy density of 33.5 kWh per kg, about 2.6 times higher than diesel, with an energy density of 13 kWh per kg[4]. The high energy content accounts for its emergence as an alternative to fossil fuels[5]. Another point is that hydrogen fuel clearly reduces carbon dioxide emissions compared to petroleum-based fuels[6]. As interest in carbon neutrality increases worldwide, the demand for hydrogen is expected to expand further, thereby highlighting the need for efficient hydrogen production systems[7].

Hydrogen is obtained through various methods, including natural gas reforming, industrial byproduct hydrogen, and water electrolysis[8]. However, the hydrogen produced as a byproduct or reformed in industrial processes is not environmentally suitable, as it consumes much energy and incurs high operational costs, limiting the achievement of carbon neutrality[9]. Water electrolysis offers a substantial way to produce cost-efficient hydrogen reducing carbon dioxide emissions[10].

Most literature informs about the overpotential of oxygen evolution reaction (OER) in relation to the complex four-electron transfer process and mechanism[11]. Thermodynamically, the onset potential for OER is set at 1.23 V [*vs.* reversible hydrogen electrode (RHE)] with a current density of 10 mA cm^{-2}. However, a higher potential is typically required to enhance the OER and subsequently increase hydrogen generation[12]. For this reason, it is essential to substitute the OER with a thermodynamically and kinetically favorable oxidation half-reaction to energy-saving hydrogen generation[13].

For example, urea, ammonia, and hydrazine are nitrogen-containing molecules that act as pollutants in the air or water. These molecules have the low theoretical onset potential of electrochemical oxidation[14]. The coupling with these anodic reactions with cathodic hydrogen evolution reaction (HER) enables the mitigation of environmental pollution while reducing the energy required to generate hydrogen[15]. Furthermore, other small-molecule oxidation reactions coupled with HER contribute to reducing the thermodynamic potential yield value-added products[16]. This approach offers the potential to produce hydrogen with lower energy requirements and an important strategy for improving its role as a sustainable energy source. As these technologies advance, more efficient and environmentally sustainable pathways for hydrogen production are expected to emerge.

Over the decades, research has focused on noble metal electrocatalysts such as platinum (Pt), Ru, and Ir. In 2009, the first Ni-based catalyst for urea electrolysis was reported, comparing its performance to Pt, Pt-Ir, and Rh[17]. For hydrazine oxidation, studies date back to 1981, with substantial efforts emerging in the 2010s[18]. In ammonia oxidation, Yao *et al.* explored Ni catalysts in alkaline solutions to assess activity[19]. Noble metals face challenges including high costs and limited industrial scalability, prompting interest in transition metals in the form of oxides, hydroxides, or chalcogenides[20]. Transition metals can also serve as active sites or supports in heterogeneous structures such as heterojunctions or 2D frameworks[21].

Ni stands out for its low cost, availability, and modifiable properties, making it suitable for large-scale applications[22]. Its surface can be engineered through heterostructures, doping, or alloying to enhance reaction kinetics and electrochemical surface area (ECSA)[23]. Doping modifies electronic structure of Ni, improving reaction dynamics. In alkaline conditions, Ni forms oxides and hydroxides, with oxidation state

changes influencing activity and stability[24]. This paper reviews recent advancements in Ni-based catalysts, providing groundwork for future designs.

General design strategies of electrocatalyst for hydrogen production

Catalyst-support interaction

Carbon-based supports such as graphene, carbon nanotubes, and nitrogen-doped carbon offer high surface area, conductivity, and tunable properties for stabilizing catalysts[25]. They anchor metal nanoparticles (NPs), nanoclusters (NCs), or single-atom catalysts (SACs), improving dispersion, stability, and activity. Functional groups (e.g., carboxyl and hydroxyl) and chemical modifications(e.g., oxidation and sulfonation) anchor catalytic metals, prevent aggregation, and improve dispersion[26]. Nitrogen doping adjusts electronic structure, increases active sites, and stabilizes catalysts via strong metal-nitrogen bonds[27]. Sulfur or phosphorus doping boosts binding energy and charge transfer. Structural defects, such as single or double vacancies, create reactive sites that enhance metal binding and dispersion[28]. Hybrid materials (e.g., graphene-carbon nanotube composites) improve surface area and mass transport, while encapsulating NPs between carbon layers prevents leaching and aggregation for long-term efficiency[29,30]. Carbon supports improve electron transfer and reaction kinetics through strong catalyst-support interactions. For instance, Ru NCs on defective graphene enhance water-splitting efficiency by increasing electron conductivity[31]. SACs on nitrogen-doped carbon demonstrate optimized atomic coordination, stabilize intermediates, and improve kinetics, with annealing and impregnation techniques ensuring robust activity[32].

Metal-based supports such as reducible oxides (e.g., CeO_2 and TiO_2) stabilize NPs, NCs, and SACs through redox properties and tunable electronic interactions[33]. Strong metal-support interactions (SMSI) modulate adsorption energies(e.g., CO, NH, and OH species) and resist deactivation[34]. Oxygen or metal vacancies in oxides anchor SACs and prevent aggregation[35]. Dopants (e.g., nitrogen and sulfur) modify electronic density and improve charge transfer, influencing reactivity and selectivity[36]. Annealing under reducing or oxidizing conditions tunes the local coordination environment, enhancing activity and stability. For instance, Ir NCs on covalent organic polymers show improved stability and activity[37].

Surface engineering

Surface modification techniques, including the introduction of defects or heteroatom doping, enhance catalytic activity by increasing the number of available reactive sites and optimizing the adsorption of reactants[38]. Creating surface defects, such as nitrogen or oxygen vacancies, optimizes the adsorption and activation of target molecules such as Ammonia, Urea, Hydrazine and their intermediates[39]. The combination of crystalline and amorphous structures allows for efficient charge separation and transfer. The crystalline domains serve as pathways for electron transport, while the amorphous domains reduce recombination losses by trapping intermediates effectively[40].

Morphology engineering

Hierarchical structures, such as porous nanoarrays, increase the surface area and improve mass transfer. Ultrathin nanosheets or nanorods expose a greater fraction of reactive edges and corners, which are more catalytically active than flat surfaces[41]. By combining a stable core with a reactive shell, core-shell catalysts reduce degradation during reactions while maximizing active site availability[42]. Hollow or tubular designs minimize diffusion resistance, allowing reactants to access active sites more efficiently[43]. Layered structures expose interlayer spaces to reactants, facilitating catalytic reactions[44].

Synergistic effects through heterostructures

Different components in heterostructures provide complementary properties, such as enhanced charge separation or optimized adsorption energies for reactants. Heterostructures create localized electrophilic and nucleophilic domains, effectively adsorbing and activating target molecules[45]. The interaction between the materials at the interface creates new electronic states, enhancing the catalytic activity by lowering the energy barriers of the reaction[46]. The heterojunction improves the charge transfer between materials through the dynamic charge redistribution improving adsorption and reaction kinetics[47].

Adjustment of electronic structure and ensemble effects

Introducing multi-metallic components and dopants, such as Co, W, Mo, Fe, or heteroatoms including N, S, and P, can effectively optimize electronic structures, facilitate charge redistribution, and lower energy barriers. Modifying charge distributions using dopants or lattice engineering can stabilize these species, improving catalytic performance[44]. The formation of high-valent nickel species, such as Ni^{3+} or Ni^{4+}, is crucial for active catalytic phases[48]. Co enhances the electron density at the Ni sites, while Mo contributes to improved hydrogen adsorption and desorption[49]. Adjusting the d-band center or density of states (DOS) optimizes the adsorption and desorption of reactants and intermediates. For example, in $NiMoO_3S$, sulfur doping improved electron transfer efficiency and urea adsorption by shifting the DOS closer to the Fermi level thereby increasing carrier concentration and facilitating electron transport[50].

Electrochemical measurement and performance evaluation criteria

Electrochemical measurements for urea oxidation reaction (UOR), ammonia oxidation reaction (AOR), hydrazine oxidation reaction (HzOR), and small molecule oxidation (SMOR) typically involve cyclic voltammetry (CV), linear sweep voltammetry (LSV), chronoamperometry (CA), chronopotentiometry (CP), and electrochemical impedance spectroscopy (EIS)[51-54].

CV and LSV tests, conducted with or without the target substance, assess activity overpotentials and compare catalytic performance, often normalized to ECSA. Lower overpotentials at 10 mA/cm^2 or 100 mA/cm^2 indicate better performance. CA and CP tests evaluate long-term stability at current densities ranging from 10 mA/cm^2 to 1 A/cm^2 or higher, over at least ten hours. EIS analyzes charge transfer and surface dynamics, with the x-intercept of the Nyquist plot showing electrolyte impedance and the high-frequency arc indicating charge transfer impedance[52]. For UOR, high-frequency responses reflect Ni^{2+}/Ni^{3+} interconversion, while low-frequency responses correspond to direct urea oxidation[55]. EIS also reveals COx generation and desorption as rate-limiting steps, with arc shifts indicating surface poisoning and stability[56].

Oxidation reactions must occur at lower overpotentials than OER, within a favorable potential region preceding OER onset. By detecting the amount of product generated within this region, key metrics such as selectivity (%), yield (%), and faradaic efficiency (FE, %) can be calculated by[52]:

$$\text{Selectivity}(\%) = (n_{product} / n_{consumed\ substance}) \times 100\% \quad (1)$$

$$\text{Yield}(\%) = (n_{product} / n_{initial\ substance}) \times 100\% \quad (2)$$

$$\text{FE}(\%) = (n_{product} \times n \times F/Q) \times 100\% \quad (3)$$

Where n, F and Q represent the number of electrons transferred, the Faraday constant (96,485 C/mol) and total electric charge (in coulombs) passed during the electrochemical formation of a specific product,

respectively. Gas chromatography (GC) and differential electrochemical mass spectrometry (DEMS) are commonly utilized techniques for detecting gaseous products. Ion chromatography (IC) is generally used to analyze ionic species, and high-performance liquid chromatography (HPLC) is used for identifying liquid-phase compounds. To enhance data accuracy and reliability, the isotope labeling method is recommended as an effective approach for tracing diverse products[57].

Energy efficiency (η) is a critical parameter in evaluating the performance of electrochemical systems. When the electrochemical conversion of the target substance is conducted on both electrodes of an electrolytic cell, η can be calculated as the ratio of the absolute value of the cell energy (E_{cell}) to the applied voltage (U), expressed as[52,58]:

$$\eta = (E_{cell} / U) \times 200\% \quad (4)$$

Here, E_{cell} is determined by the FE and the respective electrode potentials as follows:

$$E_{cell} = (FE_{anode} \times E_{anode}) - (FE_{cathodee} \times E_{cathode}) \quad (5)$$

The energy contribution (E) of each reaction is further derived from the Gibbs free energy (ΔG^0) and is determined by:

$$E = (\Delta G^0) / -nF) - 0.059 \times pH \quad (6)$$

Notably, the maximum combined FE of the system can reach up to 200%, as the contributions of the anodic and cathodic half-reactions are additive, with each capable of achieving 100%[52].

Ni-based electrocatalyst for urea oxidation reaction

Urea has been substantiated as a hydrogen carrier due to its distinctive advantages, which include nontoxicity, nonflammability, convenience in storage and transportation, and substantial hydrogen contents[51,59,60]. The thermodynamic equilibrium potential of hydrogen production using urea oxidation as an anodic reaction is only 0.37 V *vs.* RHE[61,62]. However, the UOR is a six-electron reaction [$CO(NH_2)_2 + 6OH^- \rightarrow N_2 + CO_2 + 5H_2O + 6e^-$] involving several complex processes such as continuous dehydrogenation, C-N bond cleavage, N-N coupling, CO_2 formation, and CO_2 desorption[63,64]. This complexity accentuates the need to explore Ni-based electrocatalysts as a potential solution to enhance η.

Among the catalysts utilized for the UOR, Ni-based catalysts are widely favored due to their low cost, high current density, and low overpotential in alkaline conditions[65,66]. In particular, Ni-based hydroxides are recognized as promising UOR electrocatalysts, as they form highly active oxyhydroxides in alkaline environments, enhancing their catalytic performance[67,68]. This demonstrates a strong correlation between the electrocatalytic performance of urea oxidation and the redox activity of active surfaces, bringing to light the need for further investigation into these mechanisms[56,69]. Understanding these pathways is indispensable for optimizing Ni-based electrocatalysts and improving their efficiency in the UOR.

The research to boost the efficiency of UOR focuses on maximizing catalyst activity through metal doping and novel synthesis methods and optimizing reaction pathways[51,70]. However, the mechanisms and reaction pathways of the UOR remain poorly understood. Possible mechanisms and reaction pathways have been revealed using *in situ* surface-enhanced Raman (SER) and Operando synchrotron-radiation Fourier-transform infrared (SR-FTIR) characterization techniques. *In situ* SER has been employed to

monitor active species during the UOR. For example, the formation and reduction of NiOOH species were observed as critical steps in the catalytic process, revealing that NiOOH acts as the primary active site for UOR. Operando SR-FTIR revealed bond cleavage during the UOR, identifying key intermediates such as $*NNH_2^+$ and $*OCONH_2$[71,72].

Indirect chemical oxidation mechanism:

$$Ni(OH)_2 + OH^- \leftrightarrow NiOOH + H_2O + e^- \quad (7)$$

$$[6NiOOH{\cdot}CO(NH_2)_2]_{ads} + H_2O \rightarrow 6Ni(OH)_2 + CO_2 + N_2 \quad (8)$$

Direct mechanism:

$$[NiOOH{\cdot}CO(NH_2)_2]_{ads} + 6OH^- \rightarrow [NiOOH{\cdot}CO_2]_{ads} + N_2 + 5H_2O + 6e^- \quad (9)$$

$$NiOOH + OH^- \rightarrow [NiOOH{\cdot}OH]_{ads} + e^- \quad (10)$$

$$[NiOOH{\cdot}CO_2]_{ads} + 2[NiOOH{\cdot}OH]_{ads} \rightarrow 3NiOOH + CO_3^{2-} + H_2O \quad (11)$$

$$[NiOOH{\cdot}CO_2]_{ads} + 2[OH^-]_{sol} \rightarrow NiOOH + CO_3^{2-} + H_2O \quad (12)$$

With several possible UOR pathways, this study will mainly investigate various designed compositions and structures of Ni-based electrocatalysts for UOR.

Nickel oxide and (oxy)hydroxide-based electrocatalyst for UOR (NiO, NiOOH, and NiOH)

The UOR mechanism in alkaline environments, as posited by Botte, is referred to as indirect chemical oxidation. Another mechanism, called direct chemical oxidation, was proposed by several researchers[73-76]. In the indirect mechanism, NiOOH is first electrochemically oxidized and then reduced back to $Ni(OH)_2$, indicating that NiOOH acts as an oxidizing agent to oxidize urea[77-79]. Since the Ni in the catalyst regenerates to its initial state (Ni^{2+}) after the oxidation reaction process, it exhibits sustained catalytic activity[80]. In the direct mechanism, urea undergoes electrochemical oxidation facilitated by NiOOH, thereby preserving the integrity of the active NiOOH species[56].

Ni-based (oxy)hydroxides such as NiO, $Ni(OH)_2$, NiOOH, and Ni-based layered double hydroxides (LDH) have demonstrated good catalytic performance for the UOR. For instance, Liu *et al.* reported a study on growing Ni Manganese (Mn) LDH on carbon fiber cloth (CFC). The nanoarray structure provides numerous active sites, enhancing catalytic activity[81]. Due to the presence of Mn, the oxidation peak of Ni to Ni^{3+} occurs at a lower voltage compared to $Ni(OH)_2$[81-83]. Additionally, U-NiMn LDH exhibits superior electrocatalytic performance compared to bulk NiMn LDH by exposing more catalytic active sites. U-NiMn LDH was fabricated using a hydrothermal method on CFC [Figure 1A]. Atomic force microscopy (AFM) confirmed that the catalyst forms a nanosheet structure with a thickness of 5.5 nm to 5.7 nm, highlighting the structure of U-NiMn LDH.

The honeycomb shape enhances catalytic activity by providing a large surface area, numerous active sites, and high conductivity[84,85]. The transmission electron microscopy (TEM)-energy-dispersive X-ray spectroscopy (EDS) spectrum of NiMn-LDH/CFC revealed an atomic ratio of approximately 2.97:1 (Ni),

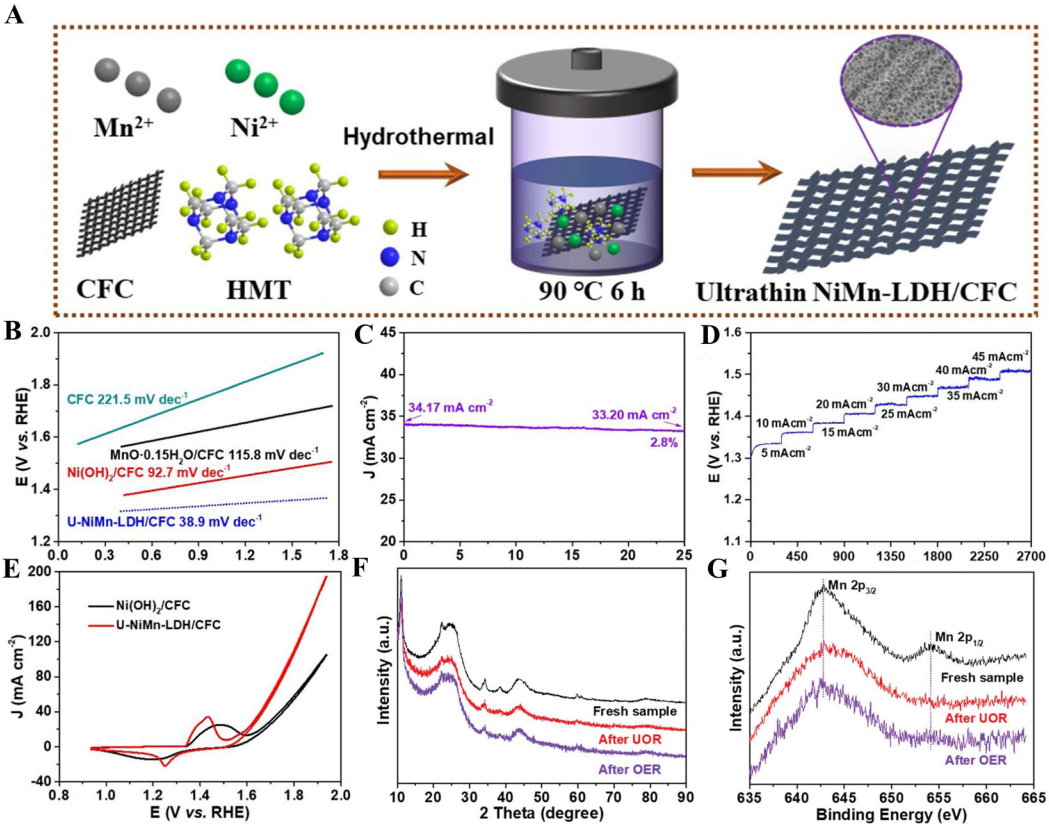

Figure 1. Examples of Ni-layered double hydroxide catalysts. (A) Scheme of synthesis of the Ultrathin NiMn-LDH/CFC; (B) Corresponding Tafel slopes; (C) UOR stability evaluates the U-NiMn-LDH/CFC; (D) Multi-current process acquired with the U-NiMn-LDH/CFC catalyst; (E) CV curves of U-NiMn-LDH/CFC and B-NiMn-LDH; (F) XRD patterns of U-NiMn-LDH/CFC before and after long-term stability test of UOR and OER; (G) Mn 2p in U-NiMn-LDH/CFC before and after long-term durability tests of UOR and OER[81]. This figure is quoted with permission from Liu *et al.* LDH: Layered double hydroxides; CFC: carbon fiber cloth; UOR: urea oxidation reaction; CV: cyclic voltammetry; XRD: X-ray diffraction; OER: oxygen evolution reaction.

consistent with the atomic ratios typically observed in LDHs. In this study, the U-NiMn-LDH/CFC catalyst demonstrated UOR activity at 1.351 V (*vs.* RHE) with a current density of 20 mA cm^{-2} in a 1.0 M KOH solution containing 0.5 M urea, showing superior performance compared to commercial RuO_2 (1.443 V). Additionally, the oxidation potential of the UOR was 272 mV lower than that of the OER, confirming that the UOR is a more thermodynamically favorable reaction. The U-NiMn-LDH/CFC catalyst exhibited a Tafel slope of 38.9 mV dec^{-1} [Figure 1B], indicating fast UOR kinetics, and maintained a current density of 34 mA cm^{-2} with only a 2.8% decrease over 25 hours [Figure 1C], demonstrating excellent stability. Additionally, stable potential levels at varying current densities in a 1.0 M KOH and 0.5 M urea solution highlighted its effective mass transport capabilities [Figure 1D]. The CV curves of $Ni(OH)_2$/CFC and U-NiMn-LDH/CFC electrodes show that the $Ni(OH)_2$ nanosheet array exhibits an oxidation peak at 1.482 V (*vs.* RHE), corresponding to the transition from $Ni(OH)_2$ to NiOOH [Figure 1E]. This transition is enhanced by the introduction of highly charged Mn^{3+} ions[86]. The results suggest that the *in-situ* generated NiOOH during the anodic reaction serves as active sites for UOR[87].

After long-term electrocatalysis for the UOR, characterization of U-NiMn-LDH/CFC using scanning electron microscopy (SEM), TEM, X-ray diffraction (XRD) analysis, Raman spectroscopy, and X-ray photoelectron spectroscopy (XPS) confirmed structural and compositional stability. XRD data showed the main peak remained stable, while SEM and TEM images confirmed the nanosheet structure was intact. XPS

data identified Ni, Mn, and O with Ni 2p peaks shifting slightly, indicating higher oxidation states post-UOR, supported by increased O 1s signals[41]. Raman spectra showed new peaks at 476 cm^{-1} and 559 cm^{-1}, linked to Ni-O vibrations indicating NiOOH formation. Mn 2p peaks remained stable, suggesting minimal valence change[88,89][Figure 1F and G].

The high activity of Ni-based electrocatalysts in UOR is primarily attributed to a combination of key factors. The presence of Mn^{3+} in the catalyts enhances the electronic structure, facilitating the conversion of Ni^{2+} to Ni^{3+}, which improves the electrocatalytic activity for the UOR[90]. The generated Ni species during the oxidation reaction play a significant role in urea electrolysis. Based on these analyses, Ni-based LDH not only generates active NiOOH species during urea oxidation but also provides an active site without precious metals[91]. A similar example is the heterostructure studied by Yan *et al.*, in which the Ni Cobalt(Co) LDH exhibits low onset potential and high activity, attributed to the abundant NiCo LDH-$NiCo(OH)_2$ interface and the dual metal characteristics[92].

Ni-based electrocatalysts have researched various strategies to improve UOR performance, particularly by engineering Ni-based oxides, hydroxides, and LDH. These strategies include morphological design, heteroatom doping, and surface engineering. For instance, Miao *et al.* demonstrated that dual cation modification using Co and Mn significantly enhances the catalytic activity and stability of Ni hydroxide [$Ni(OH)_2$] nanosheets[93].

Additionally, Periyasamy *et al.* demonstrated that spinel NiMn oxide, particularly $Ni_{1.5}Mn_{1.5}O_4$, exhibits superior electrochemical activity and low charge transfer resistance compared to other compositions, confirming its potential as an effective UOR catalyst[94]. Furthermore, Periyasamy *et al.* demonstrated that surface structure engineering of two-dimensional $Ni(OH)_2$ nanocrystals contributes to improved UOR performance, achieving optimal results by utilizing specific KOH concentrations during synthesis[94]. The advancements in $Ni(OH)_2$-based catalysts offer promising solutions for efficient urea conversion and hydrogen production, contributing to the progress of sustainable energy technologies[95].

Nickel-based chalcogenides and phosphides electrocatalyst for UOR (NiS, NiSe, and NiP)

Ni-based catalysts are commonly used in the UOR, with NiOOH acting as a key species. NiOOH is either directly or indirectly involved in the conversion of urea into N_2 or CO_2. Therefore, the aim of using Ni-based catalysts is to enhance UOR efficiency by promoting the formation of NiOOH[96,97]. However, these materials have limitations in electronic conductivity[98]. For this purpose, Jiang *et al.* have introduced Ni_2P, a highly conductive material, as a promising alternative for LDH[99] [Figure 2A and B]. Ni_2P nanoflakes have proven effective for UOR, showing high activity at 1.33 V (*vs.* RHE) with *in-situ* generated NiOOH acting as active sites. Catalytic tests in 1 M KOH with 0.5 M urea confirmed performance. Synthesized by heating β-$Ni(OH)_2$ with NaH_2PO_2 in an argon atmosphere at 300 °C for two hours, the Ni_2P nanoflakes retained their 10 nm flake structure, with uniform Ni, P, and O distribution verified by scanning transmission electron microscopy (STEM)-EDS and high-resolution (HR) TEM [Figure 2C-E] [100].

XPS analysis of Ni_2P nanoflakes shows Ni 2p peaks indicating Ni^{2+} in Ni-O/Ni-PO_4^{3-} bonds, with Ni-P peaks at lower binding energies, suggesting that Ni ions in Ni_2P are more negatively charged and enhance electron transfer [Figure 3A and B]. The P 2p spectrum confirms Ni_2P formation with P-O bonds, while O 1s reveals surface oxidation, supported by STEM-EDS mapping [Figure 3C and D].Compared to β-$Ni(OH)_2$, Ni_2P nanoflakes demonstrate a lower onset potential [1.33 V (*vs.* RHE)] and higher current density (95.47 mA cm^{-2})[100,101].

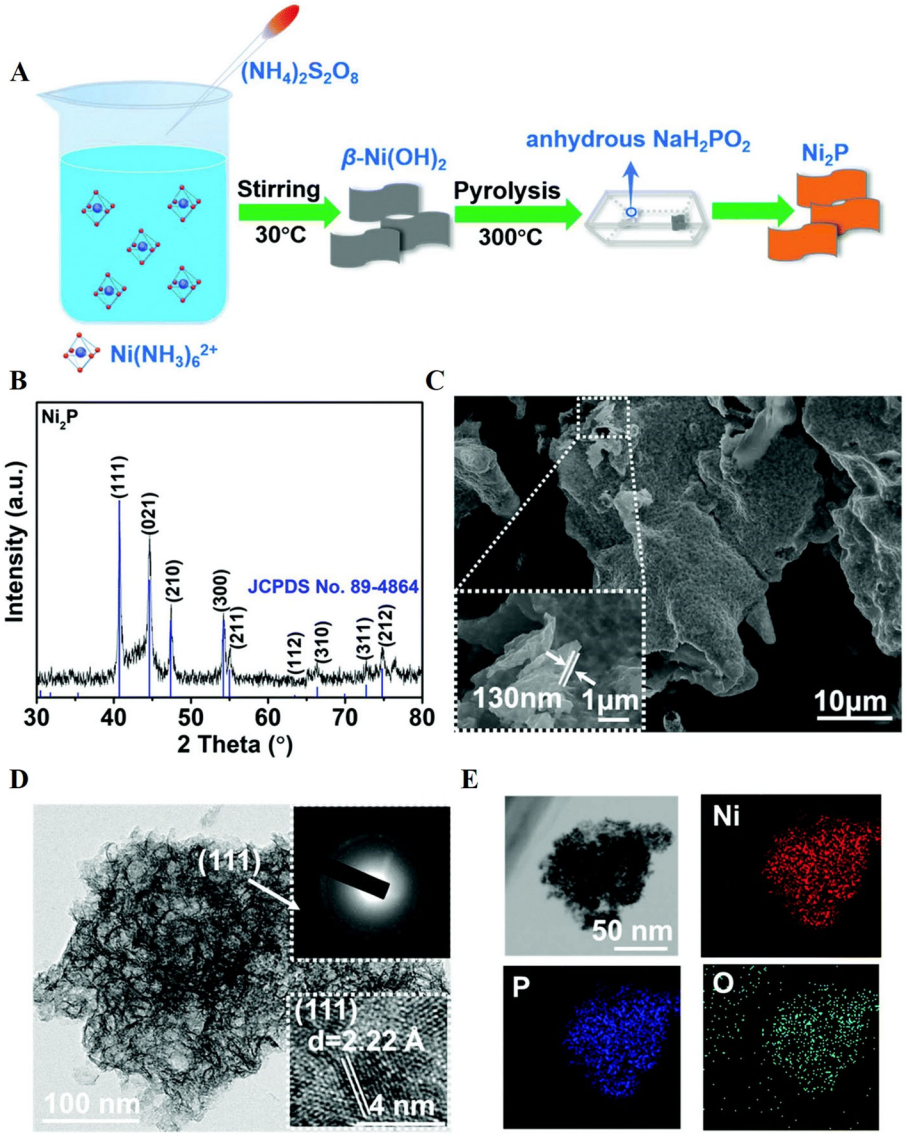

Figure 2. (A) Synthesis of Ni_2P nanoflakes; (B) XRD pattern; (C) SEM image; (D) TEM image (inset shows the corresponding HRTEM image and SAED pattern); and (E) STEM-EDS elemental mapping shows uniformity of elemental[100]. This figure is quoted with permission from Liu *et al.* XRD: X-ray diffraction; SEM: scanning electron microscopy; TEM: transmission electron microscopy; HRTEM: high-resolution TEM; EDS: energy-dispersive X-ray spectroscopy; SAED: selected area electron diffraction.

The stability of Ni_2P nanoflakes during UOR was confirmed by CP, showing minimal potential shifts. Rotating ring-disk electrode (RRDE) tests revealed superior UOR performance for Ni_2P compared to OER. Ni_2P promotes NiOOH formation via PO_4^{3-}, enhancing catalytic activity. While β-$Ni(OH)_2$ generates more NiOOH, Ni_2P enables efficient recovery of $Ni(OH)_2$, supporting a direct UOR pathway, as confirmed by ECSA analysis. This direct oxidation pathway, along with *in-situ* NiOOH generation, contributes to superior UOR performance of Ni_2P compared to the indirect pathway in β-$Ni(OH)_2$ [Figure 3E and F]. The mechanism of Ni_2P during the UOR is illustrated in Figure 3G[100].

Recently, Ni-based catalysts coordinated with diverse anions have garnered attention due to their excellent electrical conductivity and adjustable electronic configurations. Among them, Ni_3S_2 has good durability and

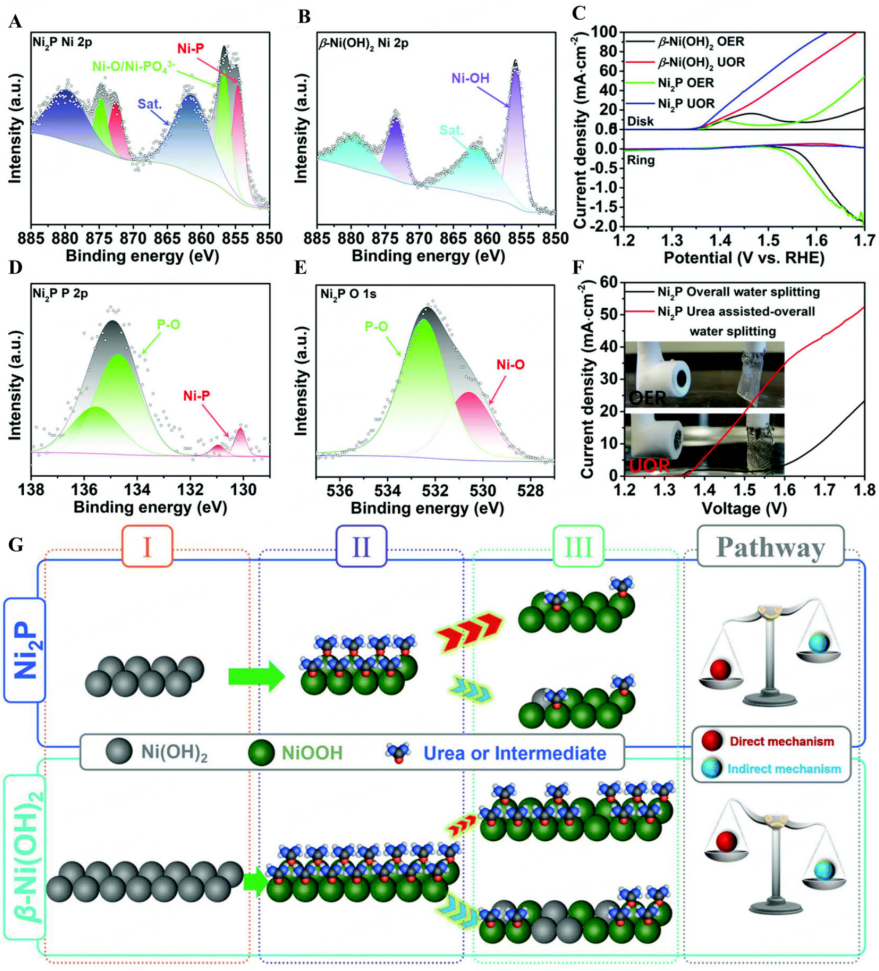

Figure 3. XPS spectra, (A) Ni 2p XPS spectrum for Ni2P nanoflake; (B) Ni 2p XPS spectrum for β-Ni(OH)$_2$; (C) p 2p XPS spectrum for Ni2P nanoflakes; (D) O 1s XPS spectrum for Ni2P nanoflakes; (E) RRDE polarization curves in 1 M KOH solution at 1,600 rpm with and without 0.5 M urea at 5 mV s^{-1} and the ring potential is set as 0.2 V (*vs.* RHE) to detect the as-generated O_2; (F) Polarization curves of the two-electrode water splitting systems with Pt mesh||Ni_2P electrodes in 1 M KOH solution with and without 0.5 M urea at 5 mV s^{-1} (G) UOR mechanism on Ni_2P and β-Ni(OH)$_2$ nanoflakes in alkaline media[100]. This figure is quoted with permission from Liu *et al.* XPS: X-ray photoelectron spectroscopy; RRDE: rotating ring-disk electrode; UOR: urea oxidation reaction; RHE: reversible hydrogen electrode.

metallic conductivity[102]. Zeng *et al.* have developed various Ni sulfides, some of which exhibit enhanced catalytic activity due to improved electronic structure achieved by doping with P and Mo [Figure 4A and B]. This study addresses a strategy to accelerate NiOOH production through an *in-situ* method to phosphorylate the surface of Ni sulfide to improve the efficiency of urea electrolysis[103]. Surface phosphorylation facilitates proton transfer, optimizes electronic structure, and increases active sites by introducing phosphate groups that act as proton acceptors. These modifications accelerate NiOOH formation and improve the urea oxidation kinetics, thereby enhancing overall electrolysis performance[104] [Figure 4C].

Ni-based electrocatalyst for ammonia oxidation reaction

Ammonia (NH_3) exhibits a high hydrogen density, making it an excellent candidate for use as a hydrogen carrier, with a hydrogen content of approximately 17.6% by weight[105]. Its molecular structure allows efficient hydrogen storage, providing an effective method for storage and transportation. Furthermore, the

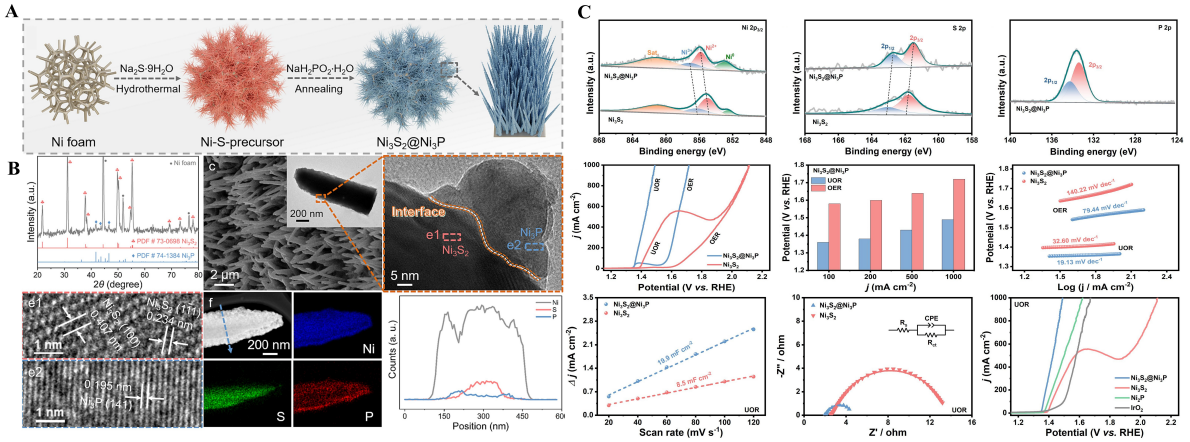

Figure 4. (A) Scheme of Ni-based sulfide; (B) XRD, SEM, TEM and HAADF-STEM image of Ni_3S_2@Ni_3P and line scanning profile of NI_3S_2@Ni_3P; (C) Confirm the performance and valence state of Ni, S and P[104]. This figure is quoted with permission from Guo *et al.* XRD: X-ray diffraction; SEM: scanning electron microscopy; TEM: transmission electron microscopy; HAADF-STEM: high-angle annular dark-field scanning transmission electron microscopy.

absence of oxygen eliminates the danger of explosion, unlike in water electrolysis[106]. The AOR is an important process to generate hydrogen with Nitrogen at a theoretical voltage of 0.097 V (*vs.* RHE). This is significantly lower than the required voltage for water electrolysis, which is 1.23 V (*vs.* RHE)[107].

Based on the study with the Pt surface, two distinct mechanisms were postulated, depending on the timing of N-N coupling. The first mechanism involves N-N coupling occurring on hydrogenated NH_x absorbed species (Gerischer and Mauerer, G-M). The second mechanism involves N adatoms coupling with each other, where the adatoms closely interact and form a bond (Oswin and Salomon, O-S). These two mechanisms play a crucial role in enhancing the efficiency of the AOR. The study results indicate that the mechanism proposed by Gerischer and Mauerer is kinetically preferred. Additionally, research demonstrates the activity of Ni-based catalysts using an ammonia volcano plot[108,109]. Ni-based catalysts are significant due to their ability to activate N-H bonds in adsorbed species such as NH_x, which is vital for facilitating the initial adsorption of ammonia on the catalyst surface. This activation not only initiates the reaction but also enhances the stability of key reaction intermediates, preventing their decomposition during the bond formation process[110,111]. Consequently, this stabilization allows for more efficient N-N bond formation, promoting a smoother progression of the reaction. Furthermore, Ni-based catalysts optimize the thermodynamic pathways by lowering energy barriers, making the overall reaction occur more readily[108].

Nickel oxide and (oxy)hydroxide-based electrocatalyst for AOR (NiO, NiOOH and NiOH)

Ni-based catalysts, known for their excellent reactivity under alkaline conditions, are the focus of active research. Nickel oxide (NiO) significantly enhances the efficiency of ammonia electrolysis and is expected to contribute to sustainable energy production[108,112]. Although the lack of understanding of the reaction mechanisms of ammonia oxidation, Herron *et al.* suggest that Ni, due to its stability in alkaline electrolytes, is considered a potential substitute for Pt, one of the best electrocatalysts for the AOR[108]. Ni-based compounds convert to NiOOH during oxidation process, with Cu doping enhancing the AOR activity of $Ni_{(1-x)}Cu_xOOH$ [Figure 5A and B]. Doping with Cu^{2+} increases the electron density around O-O-Ni, promoting NH_3 adsorption, though performance declines at high Cu doping levels[108,113]. Based on this, Fe^{3+} was co-doped to modify $Ni_{(1-x)}Cu_xOOH$. Fe^{3+} polarizes the electron cloud, further increasing the electron density around O-O-Ni and lowering the ΔG^0 for adsorption[108] [Figure 5C and D].

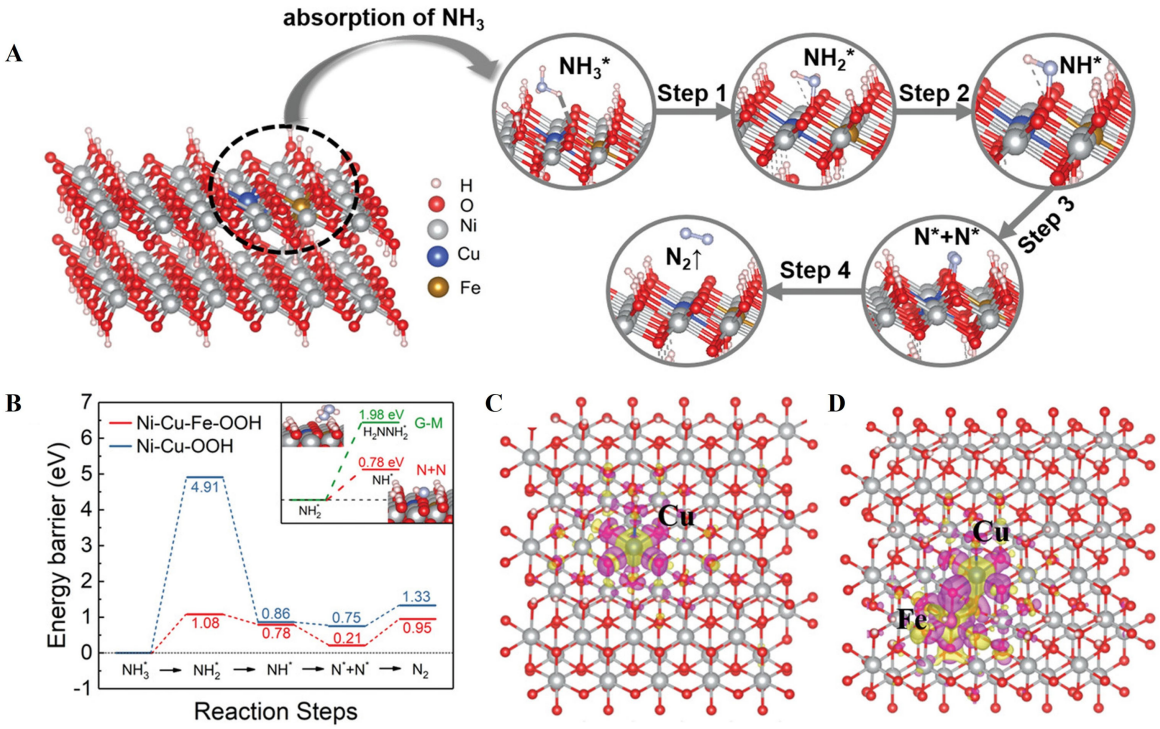

Figure 5. (A) Ni-Cu-Fe-OOH and the schematic illustration of the ammonia oxidation process; (B) The energy barriers of the different reaction steps of the N - N mechanism in Ni-Cu-Fe-OOH and Ni-Cu-OOH. The inset figure shows the energy barrier of the bifurcation step of the G-M mechanism and the N + N mechanism in the Ni-Cu-Fe-OOH system. Charge difference (C) in Ni-Cu-OOH system; and (D) Ni-Cu-Fe-OOH system (purple corresponds to charge accumulation, while yellow corresponds to charge depletion)[111]. This figure is quoted with permission from Zhu *et al.*

When both Cu and Fe are co-doped into NiOOH, the electron density around the O atoms bonded to the dopants changes, lowering the energy barrier and leading to activation that enhances AOR activity. The synthesized NiCuFe electrode achieved a 90% ammonia removal efficiency at 0.55 V after 12 h, one of the highest efficiencies reported to date [Figure 6A and B]. This study presents a valuable strategy for developing high-performance AOR catalysts. The results suggest a higher likelihood of the N-N coupling reaction occurring via the N-N coupling pathway, rather than the Gerischer and Mauerer mechanisms[108,114].

The synthesized catalysts exhibited XRD peaks similar to those of commercial NiCu bimetallic electrodes. The shift in the (111) and (200) peaks due to Fe doping indicates an expansion of the interlayer spacing, which can facilitate the accommodation of OH^- ions and potentially increase AOR activity. XPS analysis confirmed the electronic states of the surface material. Ni exhibited a distinct $2p_{3/2}$ peak at 856.7 eV, with a strong satellite peak indicating the presence of Ni^{2+}. This peak showed a shift of 0.7 eV compared to the synthesized NiCuFe/CP, suggesting that the surface Ni metal was converted to Ni^{2+}. The Cu $2p_{3/2}$ peak, located at 934.7 eV, displayed a strong satellite peak characteristic of Cu^{2+}. After activation, the Fe $2p_{3/2}$ peak appeared broad around 713.9 eV, associated with Fe^{3+}. The O 1s spectrum showed a main peak at 531.3 eV, attributed to metal hydroxides. These results confirm that the electrode surface was fully oxidized[108] [Figure 6C and D].

CV demonstrated the catalytic activity for the AOR, showing varying current densities depending on the presence or absence of NH_4Cl. The presence of Fe significantly enhanced AOR activity, as indicated by the CV data [Figure 6E]. To assess the stability of the a-NiCuFe electrode, CP was performed at 0.55 V. The

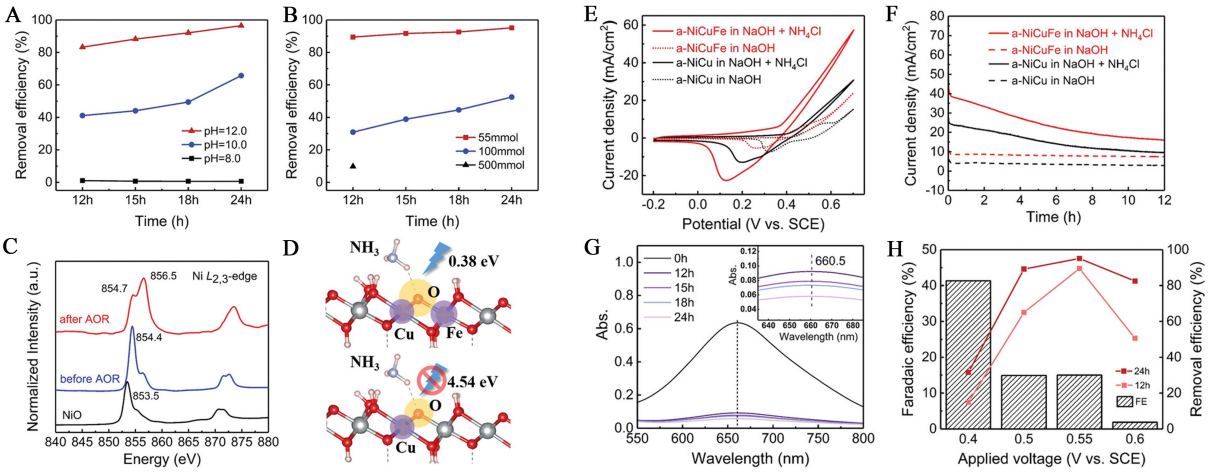

Figure 6. (A) Ammonia removal efficiency at different condition of pH and (B) different ammonia concentration; (C) XPS of XAS spectra of Ni $L_{2,3}$-edge; (D) Schematic illustration of energy barrier during ammonia adsorption on the surface of Ni-Cu-Fe-OOH and Ni-Cu-OOH; (E) CV profile and (F) Chronoamperometry curves of the NiCuFe electrode and NiCu electrode in 0.5 M NaOH w/wo 55 × 10^{-3} NH_4Cl; (G) UV-vis curves of the electrolyte tested for AOR after 12 h, 15 h, 18 h, and 24 h, respectively; (H) Ammonia removal efficiency and Faradaic efficiency of activated NiCuFe electrode under different anode potentials[111]. This figure is quoted with permission from Zhu *et al.* XPS: X-ray photoelectron spectroscopy; XAS: X-ray absorption spectroscopy; CV: cyclic voltammetry; AOR: ammonia oxidation reaction; UV: ultraviolet.

results confirmed that the a-NiCuFe electrode exhibited the highest current density under ammonia conditions, with the declining trend indicating the oxidation of ammonia [Figure 6F]. After the AOR test, the nitrate concentration in the electrolyte was measured, with no nitrite ions detected. IC revealed a nitrate concentration of 0.528 ppm, suggesting that the NiCuFe electrode facilitates N-N coupling, demonstrating its effectiveness as the AOR catalyst [Figure 6G and H]. By co-doping Cu and Fe onto NiOOH, the energy barrier is lowered, enabling efficient electrooxidation of ammonia[111].

Ni-based electrocatalyst for the hydrazine oxidation reaction

Hydrazine has been extensively used in aerospace as a propellant and rocket fuel, as a foaming agent in the synthesis of polymeric foams, as well as a precursor to pharmaceuticals, agrochemicals, and in steam cycles of nuclear and conventional power plants as an oxygen scavenger[115,116]. On the other hand, hydrazine is an exceedingly hazardous and carcinogenic compound, presenting a substantial threat to human health[117]. HzOR plays a critical role in both the elimination of hydrazine from industrial wastewater and as an alternative to the OER, minimizing the overpotential at the anode and thereby promoting a more energy-efficient route for hydrogen production[54,118]. The oxidation of hydrazine (N_2H_4) may occur via a four-electron transfer pathway through two distinct mechanisms: the alternating pathway and the distal pathway[119].

$$N_2H_4 \rightarrow {}^*N_2H_3 + H^+ + e^- \quad (13)$$

$${}^*N_2H_3 \rightarrow {}^*N_2H_2 + H^+ + e^- \quad (14)$$

$${}^*N_2H_2 \rightarrow {}^*N_2H + H^+ + e^- \quad (15)$$

$${}^*N_2H \rightarrow N_2 + H^+ + e^- \quad (16)$$

In the alternating pathway, the adsorption configuration of $*N_2H_2$ is HNNH*, where the NH groups alternate. In the distal pathway, the adsorption configuration of N_2H_2* is $*NNH_2$, with one nitrogen bonded to two protons.

Under acidic conditions, the theoretically calculated standard equilibrium potential is

$$NH_2NH_3^+ \rightarrow N_2 + 5H^+ + 4e^- \ [E_0 = -0.23 \text{ V } (vs. \text{ RHE})] \quad (17)$$

Under alkaline conditions, the theoretically calculated standard equilibrium potential is

$$N_2H_4 + 4OH^- \rightarrow N_2 + 4H_2O + 4e^- \ [E_0 = -0.33 \text{ V } (vs. \text{ RHE})] \quad (18)$$

Both are more negative than the potentials at which hydrazine begins to oxidize in acidic or alkaline solutions. The dehydrogenation of hydrazine to molecular nitrogen, a transformation that is seemingly straightforward, is accompanied by substantial kinetic constraints[120].

Nickel oxide and (oxy)hydroxide-based electrocatalyst for HzOR(NiO, NiOH, and NiOOH)

Ni-based electrocatalysts with suitable d-band configurations and versatile structures have gained significant attention for hydrazine oxidation (HzOR)[121]. NiO demonstrates superior performance in HzOR due to active phase formation, oxygen defects, and multi-metallic oxide structures[115,122]. Sakamoto *et al.* developed NiO/Nb_2O_5/C composites using evaporation drying and thermal annealing. Extended X-ray absorption fine structure (EXAFS) analysis revealed oxygen vacancies in the composites (ratios 8:1 and 4:1), leading to high activity, durability, and selectivity. NiO, a non-stoichiometric p-type semiconductor, thermodynamically favors Ni vacancies, reducing Ni-O coordination. Metallic Ni facilitates N-N bond breaking, while oxygen defects stabilize the electrooxidation process[123].

Ni/Fe and Ni/C oxides also demonstrate strong catalytic activity for HzOR, influenced by Ni oxidation states and metal synergies[124]. Askari *et al.* synthesized a $NiFe_2O_4$-reduced graphene oxide (rGO) nanocatalyst using hydrothermal methods, achieving 98% stability after 5,000 cycles[125]. Yang *et al.* created a NiC_2O_4-Nb_2O_5 hybrid on Ni foam via a two-step low-temperature reaction with Ni_3S_2 as a sacrificial template. Electron transfer from Ni to Nb redistributed charge within the composite, improving the rate-determining step (RDS)[126]. Before and after the OER and HzOR test, the binding energy of Ni^{2+} within the Ni $2p_{3/2}$ orbital decreases from 857.0 eV to 855.9 eV, the latter corresponding to the binding energy of $Ni(OH)_2$. Additionally, the observed minimal Tafel slope (84 mV/dec) suggests that the presence of electron-deficient Ni species at the $SNiC_2O_4$-Nb_2O_5 interface likely facilitates the adsorption of hydrazine molecules, thereby promoting highly favorable catalytic kinetics for the HzOR[127].

Ni hydroxide/oxyhydroxide ($Ni(OH)_2$/NiOOH) is a principal redox system widely used as a positive electrode in various applications[128]. LDHs, resembling two-dimensional materials, exhibit superior catalytic performance due to their unique geometry and hierarchical nanostructure, which enhance conductivity and ion transport, significantly improving HzOR activity[129]. LDHs are also effective supports, offering tunable elemental compositions[130]. Babar *et al.* synthesized a bimetallic Ni-Fe hydroxide nanoarray [$NiFe(OH)_2$-SD/NF] on Ni foam using stepwise electrodeposition. This method produced an amorphous $NiFe(OH)_2$ structure with numerous active sites and random bond orientations. Synergistic interactions between Ni and Fe, particularly the presence of Fe ions alongside $Ni(OH)_2$, greatly enhanced catalytic efficiency in alkaline HzOR. This enhancement is attributed to the facile intercalation of OH^-, facilitated by the increased porosity, structural disorder, and the presence of edge sites or defects within the $Ni(OH)_2$ matrix. Moreover,

the amorphous structure of $NiFe(OH)_2$ contains a greater number of unsaturated sites similar to those of metallic Ni, making it a highly effective catalyst for HzOR[131]. Liu *et al.* developed a ternary copper- Ni-Co LDH nanosheet array catalyst featuring sulfurization-induced and Cu-doped edge amorphization. The results indicated that the optimal concentration of the Cu dopant effectively modulated the electronic structure of the catalyst and enhanced the edge amorphization, which enriched the presence of high-valence Ni^{3+} ions. This effect is attributed to the formation of amorphous species during the sulfurization process, where Ni ions exhibit partial unsaturation, thus improving the performance in HzOR[48].

Nickel-based chalcogenides and phosphides electrocatalyst for HzOR(NiS, NiSe, and NiP)

Transition metal phosphide (MP) are highly effective electrocatalysts due to their superior electrical conductivity and rapid reaction kinetics[132]. Successive distortions in Ni phosphides arise from the interplay between metal-metal and phosphorus-phosphorus bonding. These compounds exhibit minor differences in binding energies compared to pure metals, retaining high electrical conductivity for efficient electron transport and reaction kinetics[133]. Their diverse structural phases and tunable electronic configurations contribute to significant synergistic effects[134].

A three-dimensional (3D) Ni-Co phosphide heterostructure, deposited on Ni foam (Ni-Co-P/NF), has been synthesized via a two-step hydrothermal method [Figure 7A]. Compared to CoP, the Co 2p spectra of Ni-Co-P/NF shift slightly to lower binding energies, while the Ni 2p spectra shift more pronouncedly to higher binding energies relative to NiP/NF [Figure 7B][135]. This shift suggests an increase in the ionicity of the M-P bond in bimetallic phosphides, facilitating improved electron transfer from the metal to the phosphide[135,136]. CV measurements in KOH solutions revealed redox peaks indicating MP oxidation state transitions critical for HzOR activity. When N_2H_4 was added, a new oxidation peak (A2) appeared, indicating preferential hydrazine oxidation over the MP. Peak A1 increased as N_2H_4 depleted, while reduction peak B1 disappeared, showing immediate reduction of metal phosphorus oxide (MPO_x) back to MP by N_2H_4. However, prolonged cycling with low or no N_2H_4 caused over-oxidation, leading to irreversible deactivation of Ni-Co-P/NF [Figure 7C]. The Ni-Co-P/NF system demonstrated superior HzOR performance, with low resistance and a potential of 90 mV to reach 200 mA cm^{-2}. It retained over 90% of its initial current density after 100 h of operation [Figure 7D and E]. Raman spectroscopy of Ni-Co-P/NF showed a peak at 400 cm^{-1} for the M-P bond, which weakened with increasing voltage, while a P-O bond peak at 1,020 cm^{-1} appeared, indicating MPO_x formation. When 0.1 M N_2H_4 was added, peaks for adsorbed hydrazine species emerged. During HzOR, the M-P bond weakened with increasing voltage but recovered after stopping the voltage, confirming MPO_x reduction back to MP by N_2H_4 [Figure 7F and G][135] .

A new reaction pathway for HzOR was proposed, involving N-N bond breakage in hydrazine at voltages above 0.2 V, suggesting a more complex mechanism than previously understood. At these voltages, Raman spectra revealed increased peak intensity for NH_2, indicating the accumulation of the $*NH_2$ intermediate from N_2H_4 bond cleavage. This new pathway (Path II) suggests that N_2H_4 adsorbs on the Ni-Co-P/NF surface, breaking into two $*NH_2$ groups, which then dehydrogenate to produce N_2[135,137]. The traditional proton-coupled electron transfer (PCET) process (Path I) remains the primary HzOR mechanism. However, Path II, involving N-N bond cleavage, becomes favorable at potentials above 0.2 V, where stronger binding of N atoms to the catalyst surface significantly reduces the N-N bond energy barrier (ΔG = 0.065 eV). This facilitates N-N bond weakening, enabling Path II to complement the PCET process [Figure 7H][127,135,137].

Liu *et al.* reported the synthesis of a heterojunction catalyst supported on Ni foam, consisting of amorphous Ni_xP and crystalline Ni NPs, using a single-step electrodeposition technique. The catalytic activity of the

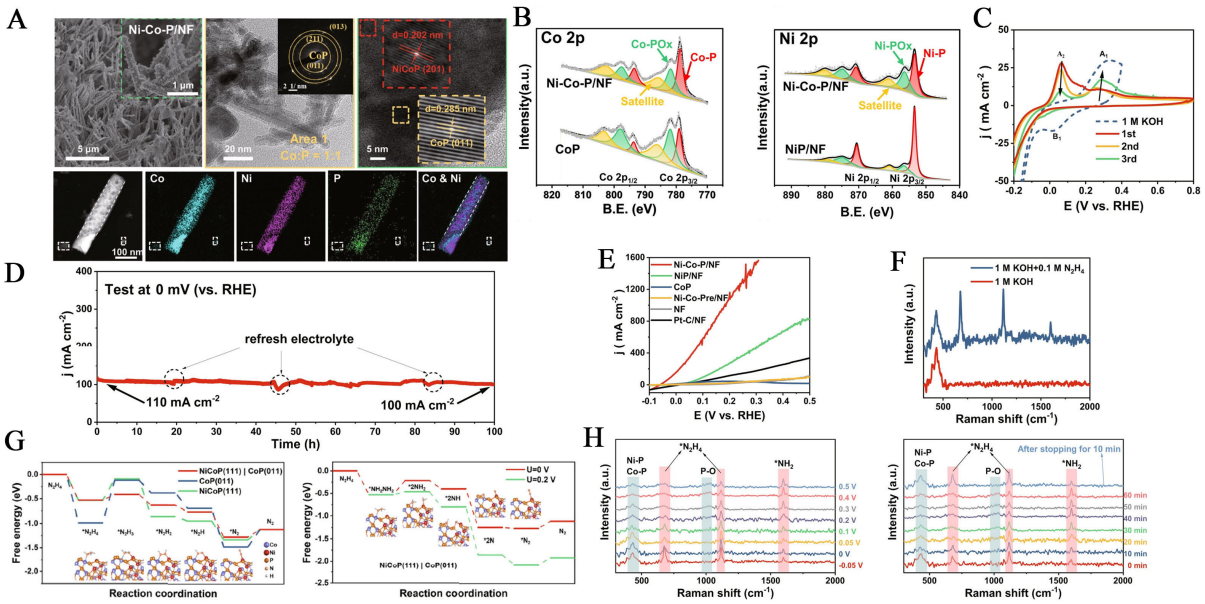

Figure 7. (A) HRTEM image of the Ni-Co-P/NF with a further magnified image in the inset; STEM-EDS elemental mapping of Ni-Co-P/NF; (B) High-resolution XPS spectra of Co 2p; c Ni 2p; d P 2p for the prepared samples; (C) CV profile in 1 M KOH (blue curves) or 1.0 M KOH + 0.005 M N_2H_4 under different cycles of scanning; (D) Stability measurements of Ni-Co-P/NF for HzOR; (E) Electrochemical properties of the HzOR in 1.0 M KOH and 0.1 M N_2H_4 50% iR-corrected LSV; (F) Raman spectra of Ni-Co-P/NF in 1 M KOH or 1 M KOH + 0.1 M N_2H_4; (G) *In situ* electrochemical Raman spectra of Ni-Co-P/NF in 1 M KOH or 1 M KOH + 0.1 M N_2H_4 at varied applied potentials and different reaction time intervals under constant 0.2 V; (H) Free energy changes of HzOR in path I at NiCoP(111)/CoP(011) interface, CoP(011) and NiCoP(111) surfaces and the most stable adsorption configuration of the intermediate at NiCoP(111)/CoP(011) interface in the inset and Free energy changes of HzOR in path II at NiCoP(111)/CoP(011) interface with the most stable adsorption configuration of the intermediate[135]. This figure is quoted with permission from Zhu *et al.* TEM: Transmission electron microscopy; HRTEM: high-resolution TEM; STEM: scanning transmission electron microscopy; EDS: energy-dispersive X-ray spectroscopy; XPS: X-ray photoelectron spectroscopy; CV: cyclic voltammetry; LSV: linear sweep voltammetry.

HzOR in an alkaline electrolyte was compared with the performance of reference catalysts, a-Ni_xP/NF and Ni/NF, under the same conditions. The a-Ni_xP /Ni/NF catalyst exhibited superior performance with an onset potential of -0.11 V and a high current density of 1,215 mA cm^{-2} at +0.30 V, surpassing the reference catalysts. EIS and CV measurements showed the catalyst had the lowest charge transfer resistance and highest double-layer capacitance, indicating a larger ECSA. When normalized to ECSA, it demonstrated 1.3 and 1.5 times higher activity than a- Ni_xP /NF and Ni/NF, respectively[40]. The superior performance of a-Ni_xP/Ni/NF is due to its heterojunction between amorphous Ni_xP and nanocrystalline Ni, offering active sites for both N_2H_4 and OH^- adsorption[40,138]. This balanced catalytic environment and the enhanced intrinsic activity of amorphous Ni_xP result in significantly higher ECSA-normalized activity compared to crystalline catalysts[138].

Metal sulfides exhibit favorable electronic properties and defect profiles, with the assembly of Ni-based heterostructures demonstrating enhanced performance due to localized modulation of the electronic structure[139]. Zhou *et al.* synthesized CoNi-alloy@CoNi-sulfide core-shell nanoarrays in a three-step process: (1) CoNi-LDH nanosheet arrays were grown on a Ni foil via a hydrothermal method, (2) the arrays were reduced to form conductive CoNi-alloy (CoNi-R) particles, and (3) a CoNi-sulfide shell was formed through *in situ* vulcanization, producing CoNi-R-S [Figure 8A]. This distinctive structure exhibits a synergistic effect, where the conductive CoNi alloy core facilitates efficient electron transfer, while the CoNi-sulfide shell presents a high density of active sites that significantly enhance the electrooxidation of hydrazine[139-141]. TEM analysis revealed the nanosheet morphology of CoNi-R-S, where the CoNi-sulfide

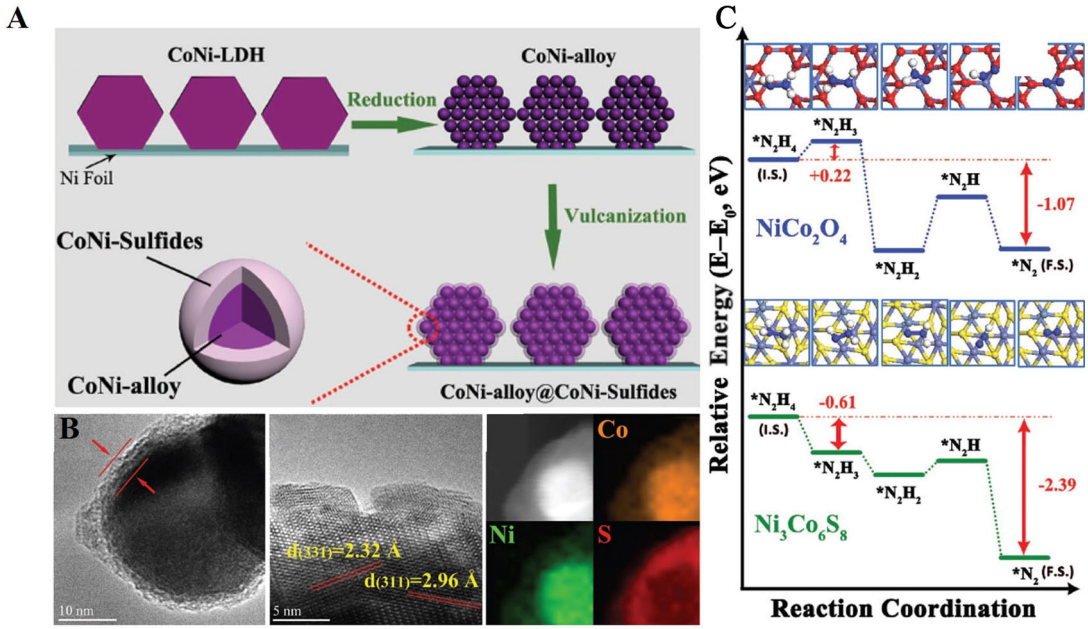

Figure 8. (A) Schematic illustration for the synthesis of CoNi-alloy@CoNi-sulfide nanoarrays (B) TEM image, crystal fringes and HAADF-STEM image and EDS mapping of CoNi-R-S; (C) The energy profiles for the reaction pathways over CoNi-sulfide and CoNi-oxide[141]. This figure is quoted with permission from Zhou *et al.* EDS: Energy-dispersive X-ray spectroscopy; TEM: transmission electron microscopy; HAADF-STEM: high-angle annular dark-field scanning transmission electron microscopy.

shell (7 nm thick) encapsulates the CoNi-alloy core (32 nm diameter). HRTEM analysis confirmed the coexistence of nanocrystalline CoNi-sulfide and CoNi-alloy. Elemental analysis verified the core-shell structure, with sulfur concentrated in the shell and Co/Ni in the core [Figure 8B]. Density functional theory (DFT) calculations showed that CoNi-sulfide has a smaller bandgap (0.75 eV) than CoNi-oxide (1.45 eV), suggesting better electron transport. The dissociation of hydrogen from N_2H_4 was more thermodynamically favorable on CoNi-sulfide, with lower activation energies for the dehydrogenation steps compared to CoNi-oxide [Figure 8C][141].

The CoNi-alloy core provides high conductivity for efficient electron transport, while the CoNi-sulfide shell offers abundant active sites for hydrazine electrooxidation. The hierarchical structure also facilitates mass diffusion and electrolyte penetration, contributing to the superior catalytic performance[141,142].

Metal nitrides exhibit exceptional catalytic efficiency across various reactions, particularly in the HzOR, due to their metallic properties, high electrical conductivity, and strong chemical stability and structural integrity[141]. The incorporation of nitrogen into Ni nitride alters the electronic properties of metals by increasing the electron density on its surface. This modification enhances electrocatalytic activity by improving the adsorption of intermediates[143]. Recently, molybdenum-doped Ni nitride (Mo-Ni_3N) porous nanosheets grown on Ni foam (Mo-Ni_3N/Ni/NF) were synthesized. The synergistic effects of interfacial engineering and chemical substitution in the molybdenum-doped Ni nitride demonstrated exceptional electrocatalytic properties for HzOR under alkaline conditions. The XPS survey confirmed Mo, Ni, and N in the Mo-Ni_3N/Ni/NF sample, with no Mo in undoped Ni_3N/Ni/NF, indicating successful Mo doping. The Ni 2p spectrum showed metallic Ni, Ni nitrides, and Ni^{2+} due to surface oxidation, with a 0.1 eV shift suggesting electron transfer between Mo and Ni. The N 1s peak at 397.2 eV indicated a metal-N bond, shifted by 0.5 eV, confirming Mo-Ni interaction. Mo 3d peaks revealed Mo^{3+}, Mo^{4+}, and Mo^{6+} states, and Ar^+ etching confirmed Ni_3N presence by leaving only metallic Ni and Ni_3N peaks [Figure 9A]. Mo- Ni_3N/Ni/NF

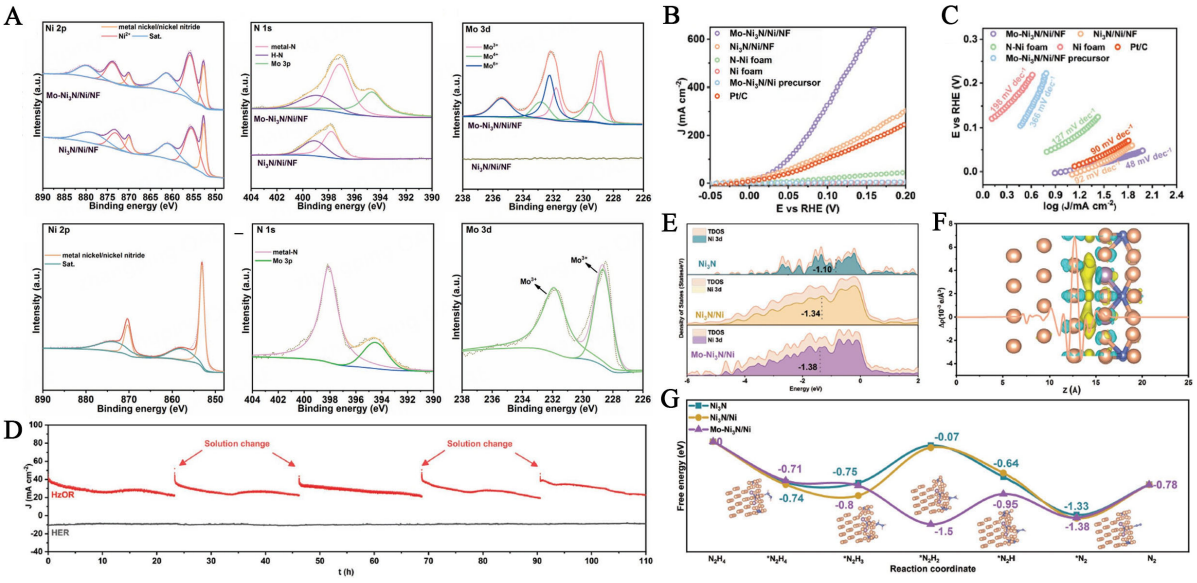

Figure 9. (A) XPS spectra performed on the Mo/Ni_3N/Ni and Ni_3N/Ni powder scratched off the Ni foam. High-resolution XPS spectra of Mo/Ni_3N/Ni for (A) Ni 2p, (B) N 1s, and (C) Mo 3d, respectively; High-resolution XPS spectra of Mo/Ni3N/Ni after Ar ion etching for Ni 2p, N 1s and Mo 3d, respectively; (B) The investigation on HzOR and HER activity for Mo/Ni_3N/Ni/NF LSV curves and (C) Tafel plots of different catalysts toward HzOR (D) I-t test for Mo/Ni_3N/Ni/NF toward HzOR (up) measured at the work potential of 124 mV and HER (down) at the work potential of 68 mV, both without iR correction; (E) The density of states and (F) Charge density difference and planar-averaged electron density difference of Mo-Ni_3N/Ni; (G) Gibbs free energy profiles for the stepwise dehydrogenation process of N2H4 with solvent interactions on Mo-Ni_3N/Ni, Ni_3N/Ni, and Ni_3N[144]. This figure is quoted with permission from Liu *et al.* XPS: X-ray photoelectron spectroscopy; HER: hydrogen evolution reaction; LSV: linear sweep voltammetry.

exhibited superior catalytic activity for HzOR in alkaline media, outperforming Ni_3N/Ni/NF. It achieved a working potential of -0.3 mV to reach a current density of 10 mA cm^{-2}, and only 75 mV was needed for 200 mA cm^{-2}. The Tafel slope was much lower for Mo- Ni_3N/Ni/NF (48 mV dec^{-1}) compared to Ni_3N/Ni/NF (92 mV dec^{-1}), indicating faster catalytic kinetics. Furthermore, Mo-Ni_3N/Ni/NF exhibited outstanding stability in HzOR. CA tests showed no significant current decay during 110 h of continuous operation, confirming the robustness of the catalyst [Figure 9B-D]. DFT simulations showed that Mo doping reduces the energy barrier for the dehydrogenation of hydrazine. The RDS for HzOR shifted from the dehydrogenation of $*NH_2NH_2$ to $*N_2H_2$ on Ni_3N to the final N_2 release on Mo- Ni_3N/Ni, reducing the energy barrier and enhancing catalytic efficiency[144]. The synergy between Mo doping and the Ni/Ni_3N heterostructure improves HzOR activities[144,145]. The DOS analysis revealed increased charge carrier density at the Fermi level, improving the electronic conductivity and charge transfer kinetics of the catalyst [Figure 9E-G][144].

Similarly, incorporating copper can significantly modify the electronic configuration and improve the adsorption energy of intermediates, thereby accelerating catalytic kinetics. Porous nanosheets of copper-Ni nitride (Cu_1Ni_2-N), anchored onto CFC, were synthesized using CuNi-LDH as a precursor through a thermal ammonolysis process. Specifically, the Cu_1Ni_2-N electrode exhibits an overpotential of 71.4 mV at a current density of 10 mA cm^{-2} in 1 M KOH solution, while concurrently achieving an extraordinarily low potential of 0.5 mV at 10 mA cm^{-2} for the HzOR in a 1.0 M KOH/0.5 M hydrazine electrolyte. As confirmed by both experimental results and DFT calculations, Cu_1Ni_2-N exhibits excellent electrical conductivity, facilitating rapid electron transport during electrocatalytic processes. The DOS analysis shows that the d-band center shifts downward relative to the Fermi level incorporating Cu_4N, reducing the hydrogen binding strength. Strong interfacial interactions between Ni_3N and Cu_4N likely promote charge

redistribution across the interfaces, modifying the electronic structure of the surface and enhancing the adsorption energy of reaction intermediates. This synergy effectively boosts the intrinsic catalytic activity[121].

A strong local electric field is established between electron-rich Ni_3N and electron-deficient Co_3N by systematically engineering bimetallic nitrides. The electric field is leveraged to further activate electron transfer by introducing Mn, leading to improved system performance. The closely aligned crystalline structures of Ni_3N and Co_3N establish an intrinsic conductive pathway, facilitating efficient electron transfer. From the DFT calculation, introducing Mn reduces the work function (W_f) difference between Ni_3N and Co_3N, suggesting that Mn promotes spontaneous charge transfer from Ni_3N to Co_3N. The enhanced HzOR activity exhibited by Mn@Ni_3N-Co_3N/NF was significantly more pronounced than that of other transition metal-based catalysts and even composite catalysts incorporating noble metals[146].

Heterostructured Ni-based electrocatalysts for HzOR

Electrochemical reactions occurring through heterogeneous catalysis are highly surface-sensitive, with their efficiency being strongly influenced by the surface chemical states and properties of the catalyst[147]. Consequently, heterostructure catalysts have been developed to optimize these interactions, utilizing key mechanisms such as the synergistic effect, electronic effect, surface defect effect, and multi-component synergistic effect[148,149].

Meanwhile, SACs, defined by atomically dispersed active sites and optimized utilization of metallic atoms enhance electrochemical activity[150,151]. The presence of unsaturated coordination optimizes the electronic DOS, leading to an increase in adsorption energy while simultaneously reducing the activation energy required for reactions[152]. As a specific example in the context of HzOR, Zhou *et al.* synthesized a $Ti_3C_2T_x$-MXene, with rich titanium vacancies, which served as a substrate for the immobilization of discrete Ni single atoms (SAs) via a "self-reduction" strategy [Figure 10A]. DFT computations were conducted to elucidate the origin of the elevated HzOR activity. Incorporating Ni SAs into the MXene matrix shifts the d-band center from 1.74 eV to 1.52 eV, optimizing activation energy for hydrazine oxidation. Ni SACs/$Ti_3C_2T_x$ show stronger hydrazine adsorption energy (-0.695 eV) than Ni NPs/ $Ti_3C_2T_x$ (-0.553 eV), identifying Ni SAs as the active sites. The total energy barrier for hydrazine oxidation is lower on Ni SACs (0.450 eV) than on Ni NPs (0.583 eV), making the reaction easier on Ni SACs[153]. Stabilization of $*N_2H_2$ and $*N_2H$ intermediates further promotes dehydrogenation [Figure 10B-E][153,154].

Due to their inherently superior catalytic properties, noble metals such as palladium (Pd), Pt, Rh, and Ru have been incorporated into Ni-based catalysts to enhance the catalytic efficiency of the HzOR[155]. For example, Pd atomically dispersed on bimetallic $NiCo_2O_4$ nanoplates enhances and accelerates the kinetics of hydrazine dehydrogenation. Additionally, Pd deposition occurs as NPs, NCs, or SAs on NiFe-LDHs, adjusting the d-band center and promoting stronger hybridization between Pd d-orbitals and the σ orbitals of N_2H_4 molecules. Recently, the synthesis of single-Pd-NPs-functionalized $NiCo_2O_4$ (Pd/$NiCo_2O_4$ composite) was achieved through a synergistic hydrothermal and calcination process, using 2D NiCo-LDH as the precursor. Then pulsed laser irradiation (PLI) methodology was employed to functionalize Pd NPs with diverse concentrations on the $NiCo_2O_4$ surface [Figure 10A]. The Pd/$NiCo_2O_4$-2 composite demonstrated superior electrocatalytic activity for the HzOR in an alkaline medium. Notably, it recorded a very low operating potential of -6 mV (*vs.* RHE) at a current density of 10 mA cm^{-2}, indicating excellent performance[156]. According to *In Situ*/Operando Raman spectroscopy, new peaks at 462 cm^{-1} and 530 cm^{-1} related to γ-NiOOH and at 636 cm^{-1} and 814 cm^{-1} corresponding to NH_2 signals appearing during HzOR [Figure 10F][76,157]. The formation of γ-NiOOH from Ni^{2+} to Ni^{3+} ions, facilitated by surface-adsorbed N_2H_4 intermediates, contributed to the enhanced HzOR activity. Pd NPs improved electrical conductivity and

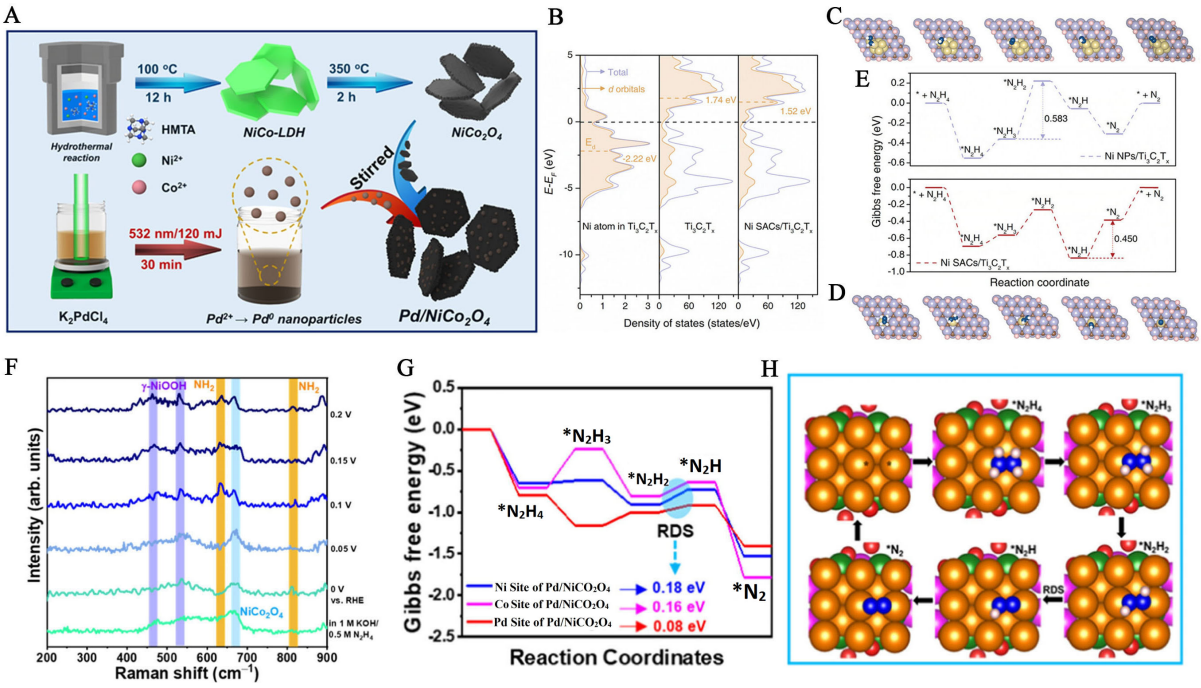

Figure 10. (A) Synthesis pathways for the Pd/$NiCo_2O_4$ composite[156]. This figure is quoted with permission from Senthil *et al*; (B) Projected electronic density of states of d orbitals and total electronic density states plots for Ni atom in $Ti_3C_2T_x$, $Ti_3C_2T_x$, and Ni SACs/$Ti_3C_2T_x$; (C) and (D) Schematic for the stepwise N_2H_4 molecular dehydrogenation process on the Ni NPs/$Ti_3C_2T_x$ and the Ni SACs/$Ti_3C_2T_x$; (E) Energy profile for HzOR on Ni NPs/Ti_3C_2Tx and Ni SACs/$Ti_3C_2T_x$[153]. This figure is quoted with permission from Zhou *et al.*; (F) *In situ*/operando Raman spectra of the Pd/$NiCo_2O_4$-2 composite during the HzOR in a 1M KOH/0.5M N_2H_4 solution at various potentials [0-0.2 V (*vs.* RHE)]; (G) Gibbs free energy plots of the HzOR on the Pd/$NiCo_2O_4$ composite catalyst. (H) Proposed HzOR process on the Pd/$NiCo_2O_4$ composite catalyst[156]. This figure is quoted with permission from Senthil *et al.* SACs: Single-atom catalysts; RHE: reversible hydrogen electrode.

promoted N_2H_4 adsorption, accelerating reaction kinetics. From the DFT calculations, the adsorption of N_2H_4 is more favorable on the Pd site (-0.79 eV) than on the Ni or Co sites[155,158]. The RDS for HzOR, dehydrogenation of N_2H_2 to N_2H, has the lowest energy barrier at the Pd site (0.08 eV), resulting in faster HzOR kinetics [Figure 10G and H][155,159].

Liu *et al.* investigated the size effect of Pd spcies at the subnanometer scale in HzOR, ranging from NPs and NCs to SAs on a NiFe-LDH, by fine-tuning precursors and reduction methods [Figure 11A][160]. Pd NCs on NiFe-LDH were found to be the most effective catalysts for hydrazine oxidation, outperforming SAs and NPs different from previous studies. Despite lower metal loading in Pd SAs/NiFe, its mass activity remained low, demonstrating that HzOR activity is more influenced by the size of Pd species than by the metal content. The order of activity is Pd NCs/NiFe > > Pd NPs/NiFe > PdSAs/NiFe. In order to elucidate the catalytic properties of the three Pd catalysts, *in situ* EIS was conducted to examine the dynamic characteristics during the HzOR. The low-frequency region in the Bode plots reflects hydrazine mass transfer. Both Pd NCs/NiFe and Pd NPs/NiFe exhibited a transition peak at 0.15 V (*vs.* RHE), indicating electrooxidation of hydrazine [Figure 11B]. However, Pd SAs/NiFe showed no transition peak, indicating poor HzOR activity[160]. The DFT calculation indicated that Pd NCs/NiFe demonstrated the best catalytic performance due to optimal electronic structure and minimal steric hindrance, allowing easier dehydrogenation steps compared to Pd SAs and Pd NPs[159,160]. Both electronic structure and steric effects significantly influence HzOR activity [Figure 11C and D][160].

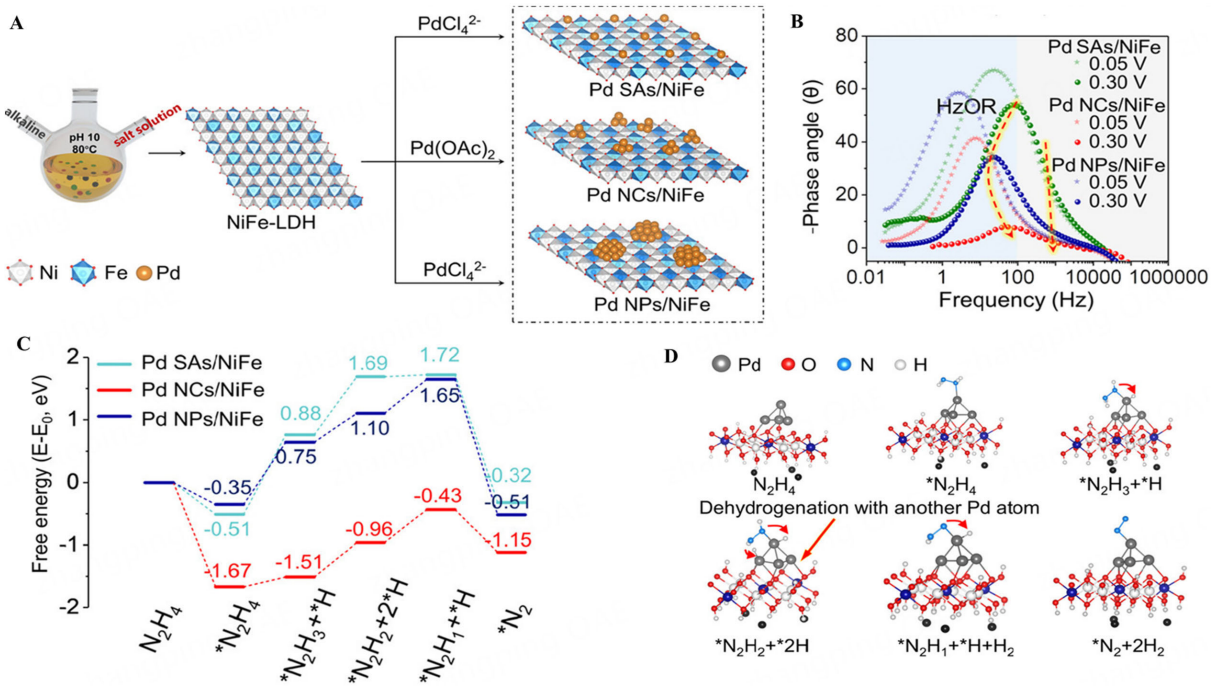

Figure 11. (A) Illustration of the Preparation of Pd SAs/NiFe, Pd NCs/NiFe, and Pd NPs/NiFe (B) Bode plots for the three Pd catalysts; (C) Reaction pathways of three Pd catalysts for the HzOR; (D) Intermediates of the HzOR for Pd NCs/NiFe[160]. This figure is quoted with permission from Liu *et al.* SAs: Single atoms; NPs: nanoparticles; NCs: nanoclusters.

Recently, partially substituting Ni with Rh within Ni-BDC [i.e., a metal-organic framework (MOF) built from Ni nodes and 1,4-benzenedicarboxylate (BDC) ligands) was synthesized. Rh atoms function as the catalytic sites facilitating hydrogen evolution, whereas Ni is accountable for the oxidation of hydrazine during the process of hydrazine oxidation-assisted seawater splitting. An exceptional level of stability was attained for the synthesized $NiRh_{0.016}$-BDC, which can be ascribed to the contractive nature of the Ni-O bond subsequent to the incorporation of Rh, thereby demonstrating that appropriate node engineering could markedly augment the long-term stability of MOF catalysts. The DFT computations indicated that the Rh nodes within NiRh-BDC can accept electrons from the neighboring Ni, thereby functioning as active sites that exhibit enhanced adsorption of H_2O^* and H^* during the HER, while the modified Ni site could facilitate a reduction in the energy barrier associated with N_2H_4 dehydrogenation as a consequence of charge transfer with proximate atomic Rh during the HzOR[161].

In the case of introduced Pt, the catalytic properties of the PtNi catalyst may arise from its interaction with hydrazine surface adsorbates, which act as intermediaries for both non-faradaic dehydrogenation and faradaic electrooxidation processes. The PtNi nanocatalyst exhibits high catalytic efficiency for the complete dehydrogenation of N_2H_4. Comparative investigations reveal that the catalytic efficiency of the $Pt_{0.2}Ni_{0.8}$ catalyst is enhanced due to its reduced particle dimensions and demonstrates superiority over alternative nanocatalysts, such as Pt, Ni, $Pd_{0.2}Ni_{0.8}$, and $Au_{0.2}Ni_{0.8}$[161].

Ru has been investigated to enhance the efficiency of the HzOR by accelerating dehydrogenation kinetics, and Ru is proposed as a potential candidate for the HER due to its hydrogen adsorption energy being comparable to that of Pt. In this regard, atomic Ni(Co)-Ru-P interfacial sites with Ru SAs (Ru1-NiCoP) were constructed on a matrix of NiCoP nanowire arrays (NWAs). According to the EXAFS data and DFT calculation, the geometric and electronic structure analyses suggest that the d-electron distribution and

energy levels in NiCoP are effectively modulated by Ru-SA, leading to improved electrocatalytic performance for HzOR[162].

Bimetallic alloys often exhibit superior catalytic performance compared to their monometallic counterparts[163]. Alloying allows for tuning of adsorption/desorption energies of reaction intermediates, often bringing them closer to optimal values for catalysis[164]. The presence of a second metal can alter the electronic structure of the catalyst surface, potentially lowering activation barriers[165]. From this perspective, NiCo/MXene was synthesized through the deposition of NiCo-MOF nanosheets onto MXene-coated copper foam, subsequently undergoing annealing in an ammonia atmosphere [Figure 12A and B]. DFT calculations explored the origin of the HzOR activity on Ni_3Co alloy. Among the facets studied (100, 110, 111), the (100) facet showed the strongest N_2H_4 adsorption with the most negative binding energy (-1.54 eV to -1.89 eV), indicating the highest activity for activating N_2H_4. Charge transfer from N_2H_4 to Ni and Co atoms weakens N-H bonds, facilitating HzOR. The dehydrogenation steps are more favorable on the (100) facet, with the RDS being the conversion of N_2H_3 to N_2H_2*, while the (110) and (111) facets face higher energy barriers during the initial dehydrogenation [Figure 12C][166].

Feng *et al.* synthesized single crystalline ultrathin Ni_xCo_{1-x} alloy nanosheet arrays (ANSAs) exhibiting finely tunable compositions (Ni_xCo_{1-x}, where x ranges from 0.9 to 0.5) through the gentle topochemical reduction of $Ni_xCo_{1-x}(OH)_2$ nanosheet array precursors under mild conditions. The remarkable electrocatalytic efficiency of ultrathin $Ni_{0.6}Co_{0.4}$-ANSA can be attributed to its exceptionally high intrinsic activity towards hydrazine oxidation, as well as its significantly increased surface area and the abundance of unsaturated atoms (i.e., surface atoms, step/corner atoms) resulting from the ultrathin two-dimensional nanostructures. These unsaturated atoms may serve as highly efficient sites for electrocatalytic activity[167]. Similarly, Sun *et al.* developed a 3D hierarchically nanotubular Ni-Cu alloy on Ni foam [Ni(Cu)/NF] for HzOR catalyst. The optimal HzOR performance of Ni(Cu)/NF is achieved with 2% Cu doping after 400 s dealloying, attributed to a large ECSA and a 3D hierarchical porous structure. This structure enhances electron transfer, mass transport, and gas release, despite the activity decreasing with further Cu dissolution[168]. Zhang *et al.* synthesized a 3D Ni-Fe alloy catalyst supported on NF using hydrothermal method and reductive calcination. The Ni-Fe/NF catalyst exhibits excellent performance in hydrazine oxidation, offering high activity, stability, and selectivity. Specifically, the influence of Fe on enhancing the HzOR activity while simultaneously suppressing the non-faradaic decomposition of hydrazine[169].

CARBON CONTAINED SMALL MOLECULE OXIDATION REACTION

By incorporating chemical compounds with lower oxidation potentials into the water electrolysis process, it becomes possible to couple thermodynamically favorable oxidation reactions with the HER, allowing the electrolytic system to achieve significant benefits at both the anode and cathode while simultaneously reducing energy consumption[129]. Additionally, certain carbon-containing SMOR can lead to the production of high-value chemicals[129]. For example, 5-Hydroxymethylfurfural (HMF) can be oxidized to the valuable product 2,5-furandicarboxylic acid (FDCA). The theoretical overpotential for the electrooxidation of HMF to FDCA can be derived from the thermodynamic considerations of the reaction. The complete oxidation of HMF to FDCA involves a six-electron transfer process[170]. This means that theoretically, six electrons are required to convert one molecule of HMF to one molecule of FDCA.

$$\text{Cathode reaction: } 6H_2O + 6e^- \rightarrow 3H_2 + 6OH^- \quad (19)$$

$$\text{Anode reaction: } HMF + 6OH^- \rightarrow FDCA + 4H_2O + 6e^- \quad (20)$$

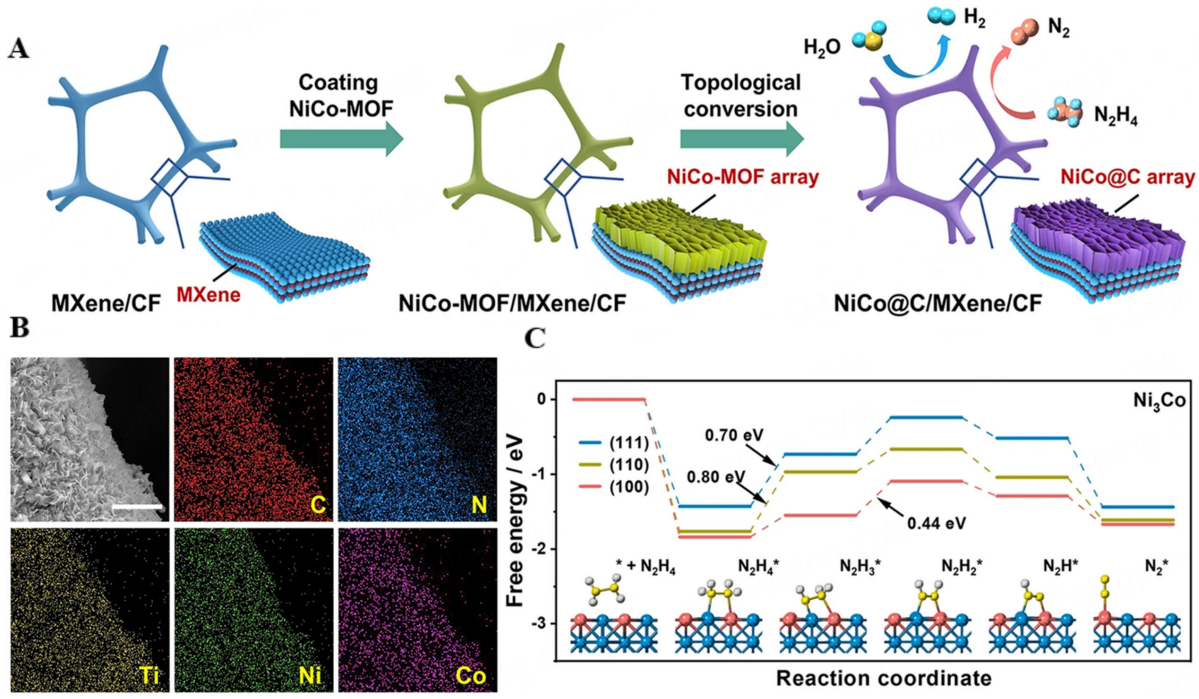

Figure 12. (A) Schematic illustration of the synthetic strategy of NiCo@C/MXene/CF; (B) Free energy profiles of stepwise HzOR on different facets of Ni_3Co alloy. Inset is the corresponding structural evolution of reaction intermediates adsorbed on the (100) facet of Ni_3Co; (C) Elemental mapping showing the uniform distribution of C, N, Ti, Ni, and Co elements in this electrode. Scale bar, 5 μm[166]. This figure is quoted with permission from Sun *et al.*

$$\text{Overall reaction: HMF} + 2H_2O \rightarrow \text{FDCA} + 3H_2 \quad (21)$$

For the overall reaction, the calculated standard reaction potential is only 0.113 V (*vs.* normal hydrogen electrode, NHE), which is much smaller than the OER[171]. The oxidation of alcohols represents a highly promising and viable candidate for engaging in substitutional reactions specifically associated with the process of OER, which is a critical aspect of various electrochemical systems and energy conversion technologies[133]. The thermodynamic potential, a crucial parameter in evaluating the energetic feasibility of chemical reactions, particularly for the oxidation of methanol (CH_3OH), is measured to be 0.103 V (*vs.* RHE)

$$\text{Anode reaction: } CH_3OH + H_2O \rightarrow HCOOH + 4H^+ \ [E_0 = 0.103 \text{ V } (vs. \text{ RHE})] \quad (22)$$

During the methanol oxidation reaction (MOR), there is potential for the generation of a valuable product, formic acid (FA), which can be synthesized through this chemical transformation[172]. Furthermore, the glycerol oxidation reaction (GOR) exhibits a minimal theoretical oxidation potential [0.003 V (*vs.* RHE)], thereby rendering it a compelling alternative to the OER for the generation of hydrogen.

$$HOCH_2CH(OH)CH_2OH + 3H_2O \rightarrow 3CO_2 + 14H^+ + 14e^- \quad (23)$$

$$HOCH_2CH(OH)CH_2OH + 3H_2O \rightarrow 3CO_2 + 7H_2 \quad (24)$$

Ni-based electrocatalysts capable of efficiently oxidizing carbon-containing small molecules, including the substances mentioned above, were investigated as suitable alternatives for the OER[173,174].

Nickel oxide and (oxy)hydroxide-based electrocatalyst for SMOR (NiO, NiOH, and NiOOH)

Most carbon-based molecules, such as various forms of alcohols and aldehydes, typically undergo nucleophilic oxidation reaction (NOR), a key mechanism in organic chemistry that involves electron transfer from a nucleophile to an electrophilic species[175,176]. Recently, the β-$Co_{0.1}Ni_{0.9}(OH)_2$/NF was synthesized for the oxidation of ethanol, phenylcarbinol, HMF, and benzylamine in NOR, producing acetic acid, benzoic acid, FDCA, and benzonitrile, respectively, with a lower theoretical potential than the OER. For β-$Ni(OH)_2$ and NiO catalysts, the activity of NOR arises from β-Ni(OH)O (from lattice oxygen) and $NiO(OH)_{ads}$ (from adsorbed oxygen), respectively. The β-$Ni(OH)_2$ operates via a unique two-step, one-electron mechanism involving lattice oxygen, suggesting that NOR activity can be optimized by adjusting the lattice oxygen environment. The β-$Co_{0.1}Ni_{0.9}(OH)_2$/NF demonstrates outstanding ethanol oxidation reaction (EOR) performance, with a low onset potential [60 mV lower than β-$Ni(OH)_2$/NF] and high current density (98 mA cm^{-2} at 1.35 V). It achieves near-complete ethanol conversion with 98% selectivity and a faradic efficiency of 95%, producing acetic acid as confirmed by GC-mass spectrometry (MS) and proton nuclear magnetic resonance (^{1}H NMR) spectroscopy [Figure 13A and B][176].

Huang *et al.* synthesized a Pd/$Ni(OH)_2$/rGO hybrid electrocatalyst in which $Ni(OH)_2$ significantly enhanced the performance of Pd for the EOR in an alkaline solution by improving both activity and durability. The catalyst maintained a high mass activity of 440 mA mg^{-1} after prolonged use, attributed to the role of $Ni(OH)_2$ in facilitating the removal of carbonaceous poisons. Additionally, $Ni(OH)_2$ reduced the selectivity for C_2 products, thereby enhancing reaction control[177].

In the case of aldehydes, Trafela *et al.* investigated a mechanism for transforming Ni nanowire (Ni-NW) electrodes, originally composed of metallic Ni coated with NiO, into a catalytically active, disordered β-NiOOH/β-$Ni(OH)_2$ redox pair with enhanced activity for HCHO oxidation. Potential cycling in 0.5 M KOH at different scan rates (0 mV s^{-1}, 10 mV s^{-1}, 200 mV s^{-1}, and 400 mV s^{-1}) modifies the electrode by forming a hydroxide layer. The optimal catalytic performance was achieved at a scan rate of 200 mV s^{-1}, yielding high current density (0.6 mA cm^{-2}), low onset overpotential (0.4 V), and a minimal Tafel slope (99 mV dec^{-1}). This enhanced performance is attributed to a balanced diffusion of OH^- and O_2, preventing NiO formation and improving conductivity of NiOOH by lowering the W_f [Figure 13C][178].

In the regards of GOR, NiCrO with vacancies (NiCrO-VCr,O) was synthesized by hydrothermal and annealing process and subsequently employed CV forming oxygen vacancies. The optimized NiCrO-VCr,O catalyst achieved impressive glycerol electrooxidation performance. *In situ* analyses (EIS, Raman spectroscopy, and attenuated total reflection (ATR) FTIR spectroscopy revealed distinct interfacial behaviors, unlike NiS_x/Ni and NiO_x/Ni nanorod arrays (NRAs), which undergo deep reconstruction to NiOOH for both OER and GOR; $NiSe_x$/Ni NRAs experience only shallow reconstruction under GOR, allowing direct glycerol oxidation at the interface [Figure 13C]. DFT calculations confirmed the enhanced adsorption of OH^- and glycerol on NiCrO-VCr,O, indicating favorable negative adsorption energies (-0.869 eV, -0.526 eV, and -1.097 eV, respectively), in contrast to thermodynamically unfavorable positive energies on NiO [Figure 13D and E][175].

A NiOOH/Ni_3S_2/NF catalyst was synthesized by electrodepositing NiOOH on Ni_3S_2 nanosheets, enhancing electron transport and glycerol adsorption. The catalyst achieved a high FE (97.7%) for FA at 1.4 V (*vs.* RHE). The TEM analysis conducted subsequent to the GOR, in conjunction with the *in situ* Raman

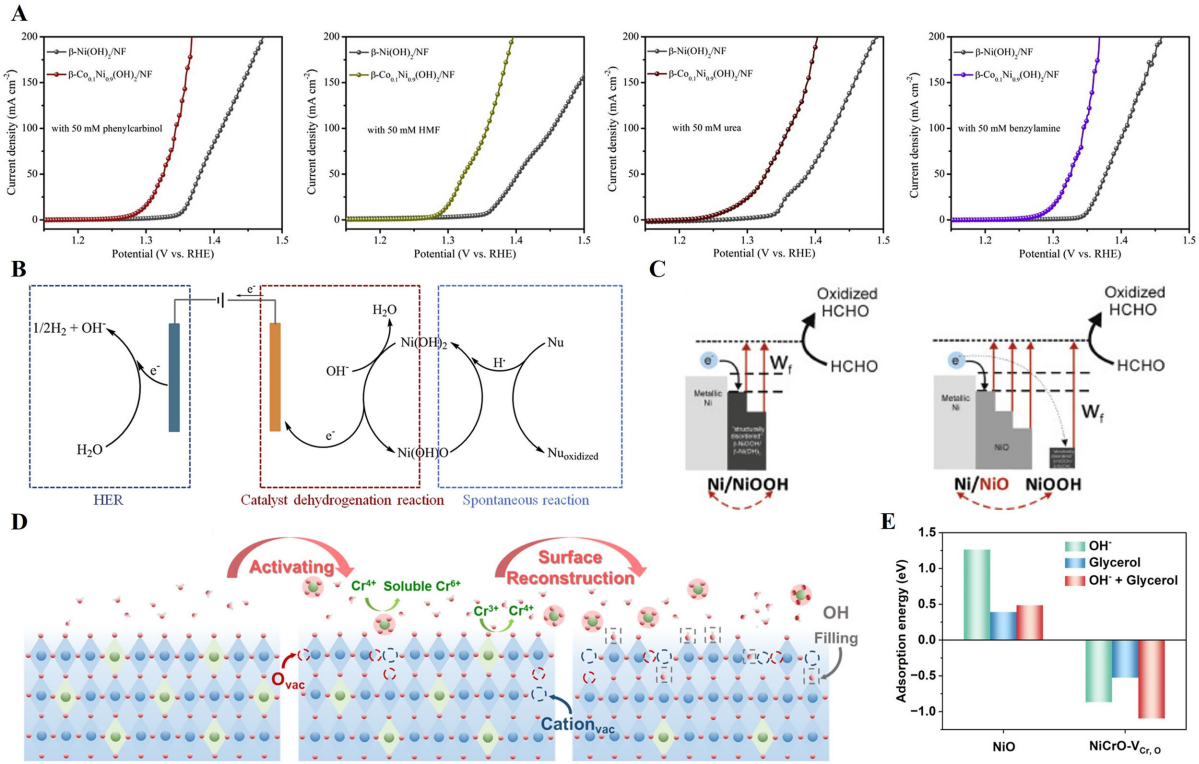

Figure 13. (A) LSV curves for b-Ni(OH)$_2$/NF and b-$Co_{0.1}Ni_{0.9}(OH)_2$/NF in 1 M KOH with 50 mM phenylcarbinol, HMF, benzylamine and ethanol. Inset shows the conversion, selectivity, and faradic efficiency of EOR for b-$Co_{0.1}Ni_{0.9}(OH)_2$/NF; (B) Proposed NOR mechanism scheme for b-Ni(OH)$_2$[176]. This figure is quoted with permission from Chen *et al.*; (C) Schematic presentation of the electron-injection mechanism for Ni-NiOOH/Ni(OH)$_2$-nanowire electrode and Ni-NiO-NiOOH/Ni(OH)$_2$-nanowire electrode; (D) Schematic diagram of the activated process[178]. This figure is quoted with permission from Trafela *et al.*; (E) Adsorption energies of OH^-, glycerol, and the co-adsorption of OH^- and glycerol on the NiO (200) surface and the NiCrO-VCr,O (200) surface[175]. This figure is quoted with permission from Xia *et al.* LSV: Linear sweep voltammetry; HMF: 5-Hydroxymethylfurfural; EOR: ethanol oxidation reaction; NOR: nucleophilic oxidation reaction.

spectroscopy investigations, provided compelling evidence which indicated that the NiOOH species served as the genuine active site throughout the GOR process. *In situ* IR and ^{1}H NMR studies identified the GOR pathway, while Raman spectroscopy revealed NiOOH formation at active sites [Figure 14A-C][179].

Nickel-based chalcogenides and phosphides electrocatalyst for SMOR(NiS, NiSe, and NiP)

Recently, the Ni-based catalyst that engages in coordination with diverse anions on Ni NRAs (NiO_x/Ni, NiS_x/Ni, and $NiSe_x$/Ni NRAs) was synthesized by the electrodeposition. $NiSe_x$ /Ni NRAs demonstrate enhanced GOR performance, achieving a FE of 92.9%. *In situ* spectroscopy elucidates that the coordination of NiSe impedes considerable oxidative restructuring, averting the formation of the NiOOH phase, consequently augmenting both the catalytic activity and stability [Figure 15A]. DFT calculations confirmed that the oxidation of $*C_2H_3O_3$ intermediates via the adsorption of H_2O is the RDS in the GOR at the $NiSe_x$ interface [Figure 15B][180].

NiS exhibits superior electrocatalytic activity for the MOR and EOR in alkaline media, due to an increased ECSA and sulfate ions on the NiOOH surface. NiS achieves FEs over 95% for formate from MOR and over 80% for acetate from EOR, with nearly double the product yield compared to Ni-only electrodes in 10,000 s tests [Figure 15A]. DFT calculations indicate that sulfate groups on the NiOOH surface enhance electroconductivity and electron transfer, favoring ethanol oxidation with a lower total reaction energy

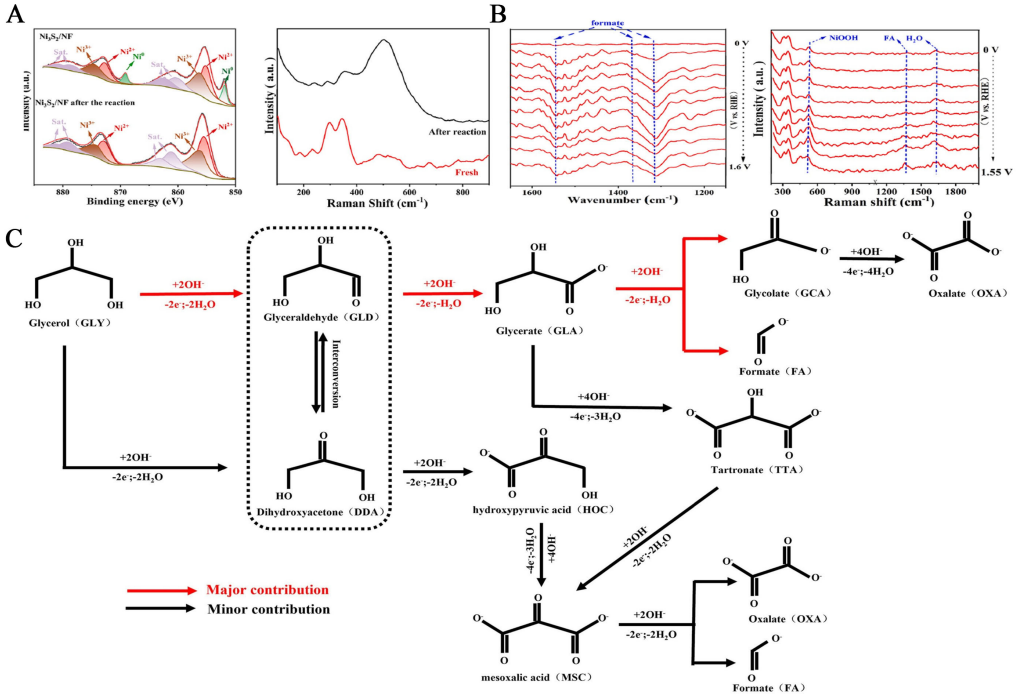

Figure 14. (A) The XPS high-resolution S 2p spectra and The Raman spectra of NiOOH/ Ni_3S_2/NF catalysts before and after the reaction; (B) The *in situ* IR spectra and the *in situ* Raman spectra of NiOOH/Ni_3S_2/NF catalysts in 1 M KOH with 0.1 M glycerol; (C) Proposed GOR pathway in alkaline media based on the NiOOH/Ni_3S_2/NF electrode[179]. This figure is quoted with permission from Xu *et al.* XPS: X-ray photoelectron spectroscopy; GOR: glycerol oxidation reaction.

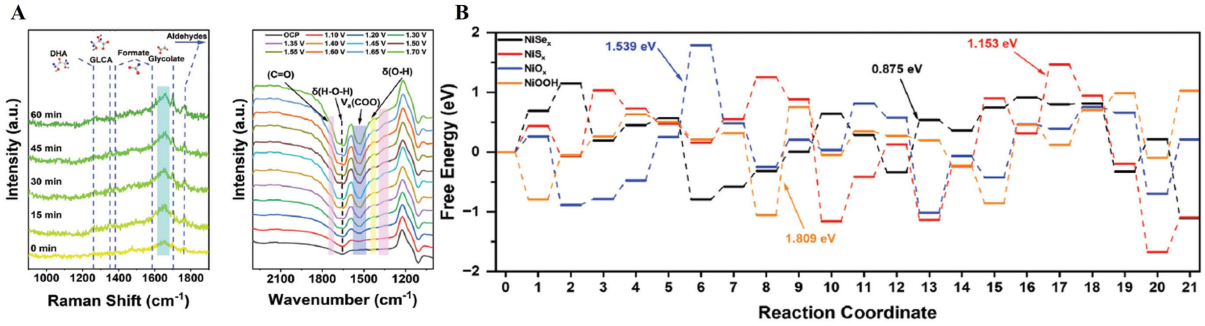

Figure 15. (A) *In situ* Raman spectra of $NiSe_x$/Ni NRAs at a constant potential of 1.35 V (*vs.* RHE) for 60 min during GOR and *in situ* ATR-FTIR spectra of $NiSe_x$/Ni NRAs for GOR collected at different potentials from open circuit potential (OCP) to 1.7 V (*vs.* RHE); (B) The calculated Gibbs free energy profiles of GOR on $NiSe_x$, NiS_x, NiO_x, and NiOOH[180]. This figure is quoted with permission from Wang *et al.* NRAs: Nanorod arrays; RHE: reversible hydrogen electrode; GOR: glycerol oxidation reaction; ATR: attenuated total reflection; FTIR: fourier-transform infrared.

(0.82 eV) than methanol (1.25 eV) [Figure 16A-C][181].

Jiang *et al.* developed the Pd-Ni-P electrocatalyst, containing Ni and P dopants, exhibits enhanced EOR activity in alkaline media due to charge transfer effects and increased active sites. Compared to Pd-Ni and Pd-blk, Pd-Ni-P has a more amorphous structure, smaller particle size, lower onset potential, and reduced overpotential by 110 mV[182].

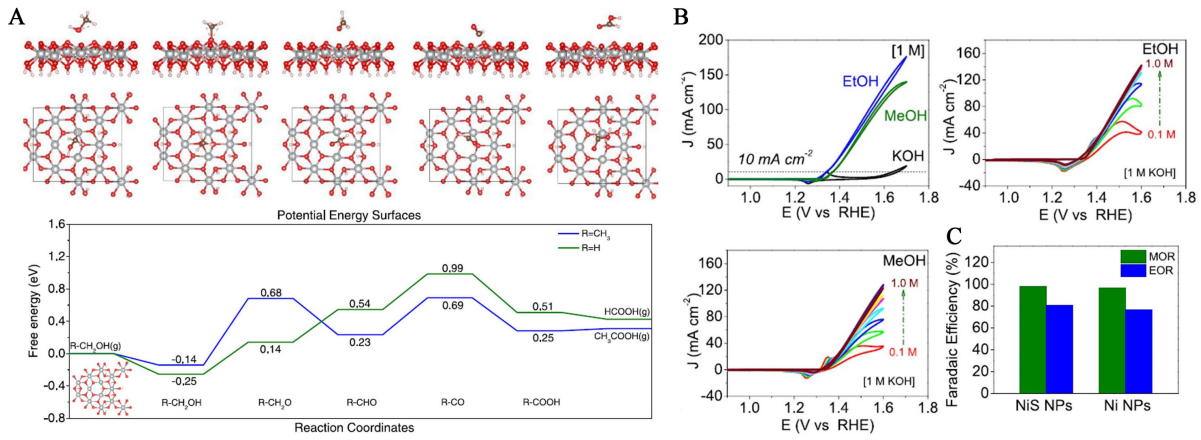

Figure 16. (A) Stable adsorption configurations of intermediates involved in the process of MOR on the NiOOH surface from the side and top view; (B) CV curves without and with 1 M methanol or ethanol at a scan rate of 50 mV s^{-1}. CV curves as a function of methanol and ethanol concentration from 0.1 M to 1 M; (C) Comparison of Faradaic efficiency between the NiS and Ni electrodes[181]. This figure is quoted with permission from Li *et al.* CV: Cyclic voltammetry; MOR: methanol oxidation reaction.

Heterostructured nickel based electrocatalyst for SMOR

Recently, Araujo *et al.* synthesized bimetallic electrocatalysts composed of Pd and Ni, followed by a comprehensive comparison of these catalysts to evaluate their kinetics in the MOR. Pd, Pd_3Ni, and PdNi catalysts exhibit different MOR behaviors due to their unique interactions with intermediates and varying CO poisoning tolerance. Pd shows lower CO tolerance, favoring early intermediates such as formaldehyde (CH_2O) over CO_2. Pd_3Ni more effectively avoids CO formation by following a pathway through CH_2OOH, resulting in higher CO_2 production and enhanced MOR efficiency. PdNi demonstrates the highest MOR activity by favoring highly oxidized intermediates (e.g., CHOO), which prevent CO formation and rely on OH^- concentration to promote direct oxidation pathways to CO_2. DFT calculations and experimental data confirm that greater OH^- adsorption of PdNi supports its superior MOR performance compared to Pd and Pd_3Ni[183].

Three bimetallic catalysts composed of Pt and Ni, designated as $PtNi_1$ through $PtNi_3$, were synthesized with differing Ni concentrations. Spectroscopic analyses revealed that surface $Ni(OH)_x$ islands form under alkaline conditions but block *OH adsorption, rendering the bifunctional mechanism inactive. Instead, Ni modulates the electronic structure of Pt, enhancing catalytic performance and promoting selective partial carbon-carbon (C-C) bond cleavage toward glycolate formation. $PtNi_2$ demonstrates the highest glycerol oxidation activity due to an optimized Pt-Ni coordination that weakens *CO and *OH binding on Pt [Figure 17A and B][184].

Nitaya *et al.* synthesized Pd NPs supported on Ni SAs encapsulated in carbon nanotubes (NiSA). The primary rationale for the pronounced enhancement in the alcohol oxidation of Pd/NiSA can be attributed to the distinctive synergetic effect exerted by the Ni SACs that effectively draw electrons from the supported Pd NPs. The Pd NPs, which possess a positive charge resulting from the elevation of the energy level of the Pd 3d orbitals, significantly extract electrons during the charge transfer mechanism, thereby promoting the cleavage of the C-C bonds[185].

CONCLUSION AND OUTLOOK

In conclusion, advancements in Ni-based electrocatalysts address challenges in energy-efficient hydrogen production. By facilitating various oxidation reactions as substitutes for OER, these catalysts reduce energy

consumption, offering a sustainable alternative to fossil fuels [Table 1].

Optimizing catalytic design involves adjusting electronic structure, surface area, and morphology to enhance performance. Metal doping or alloying modifies active sites, lowering reaction barriers in oxidation reactions such as UOR, AOR, HzOR, and SMOR. Ni-based catalysts with LDH structures excel due to their structural tunability, akin to 2D materials. For HzOR, integrating transition metals such as Co or Mn with Ni improves efficiency by modulating electronic structure and enhancing hydrazine dehydrogenation kinetics [Figure 18].

Limitations and potential solutions

Despite advancements, challenges remain. The complexity of multi-electron transfer in oxidation reactions requires further investigation to clarify mechanisms. Achieving long-term stability under harsh conditions, such as AOR and HzOR, is difficult due to catalyst degradation. While progress has been made in understanding this degradation, robust designs such as core-shell structures (e.g., conductive alloy cores with oxide or sulfide shells) show promise in enhancing stability and activity.

Future guidelines in anodic reaction development

To advance anodic reactions, challenges such as selective adsorption, byproduct formation, and competing reactions (e.g., OER) can be addressed by leveraging the versatility of nickel. For UOR and SMOR, designing multi-metal active sites tailored to specific intermediates enhances reaction kinetics. Transition metals (e.g., Ti, Fe, Cu) and noble metals (e.g., Rh, Ir, Ru) synergize with Ni, while high-entropy materials enable quaternary or quinary combinations to improve performance. Investigating Ni-metal combinations for synergetic effects remains a key focus.

For AOR and HzOR, suppressing NH_3 formation and promoting N-N coupling requires strategies such as dimeric active site design and optimizing site distances. SA dimers, sub-nanosized alloys, and partial anion substitution (e.g., N, P, S) can facilitate coupling by modulating site distances. Future research should refine synthetic methods for dimeric site formation and controlled metal or anion substitution.

Industrial perspective of promising or commercial catalyst

Mass production of electrocatalysts demands precision manufacturing techniques capable of producing millions of membrane electrode assembly (MEA) annually. For commercial electrocatalysts, production must ensure high-quality, eco-friendly catalysts using scalable methods such as roll-to-roll processing and efficient recycling. Ni-based catalysts dominate due to cost-efficiency balance, but challenges such as degradation, reverse currents, and inefficiencies at high current densities persist. Advancing MEA-level electrocatalyst design is crucial to address real-world issues such as mass transport, thermal management, and three-phase boundary interactions.

Bridging the gap between academia and practical applications

Future research should explore new material combinations and synthesis techniques to enhance the activity, selectivity, and stability of Ni-based catalysts. Machine learning (ML) facilitates high-throughput catalyst screening, reaction mechanism analysis, and structure-property relationship identification. By integrating ML with DFT, predictive precision improves while reducing discovery time and resources. Advanced ML models such as convolutional neural network (CNN) and gradient boosting regressions predict adsorption energies, reaction pathways, and optimal catalyst configurations, accelerating design under industrial conditions. Combining the computational hydrogen electrode (CHE) model with ML further refines active site identification and configuration optimization, boosting stability and efficiency. ML-trained models for Ni-based catalysts minimize trial-and-error, optimizing performance for UOR, AOR, HzOR, and SMOR applications.

Table 1. Summary of electrocatalytic performance of different applications

Catalyst	Electrolyte	Potential	Tafel slope	Stability	Reference
Ultra thin-Ni-Mn LDH	0.5 M Urea/1.0 M KOH	Overpotential = 1.351 V	38.9 mV/dec	40 h	[81]
Co and Mn co-doped $Ni(OH)_2$ nanosheet	0.33 M Urea/1.0 M KOH	Overpotential = 1.38 V	35 mV/dec	25 h	[94]
Mo/Ni-P	0.5 M Urea/1.0 M KOH	Overpotential = 1.43 V	30.2 mV/dec	12 h	[99]
Ni_2P nanoflakes	0.5 M Urea/1.0 M KOH	Overpotential = 1.6 V	30.2 mV/dec	20 h	[100]
Ni-Fe phosphide/CF	0.33 M Urea/1.0 M KOH	Overpotential = 1.39 V	30.2 mV/dec	8 h	[101]
Ni_3S_2@Ni_3P	0.33 M Urea/1.0 M KOH	Overpotential = 1.36 V	19.13 mV/dec	20 h	[104]
P-MoO_2@CoNiP	0.33 M Urea/1.0 M KOH	Overpotential = 1.38 V	47.6 mV/dec	100 h	[126]
NiCuFe electrode	0.055 M NH4Cl/0.5 M NaOH	Overpotential = 0.55 V	47.6 mV/dec	12 h	[111]
Cu1Ni_2-N/CFC	0.5 M Hydrazine/1.0 M KOH	Overpotential = 0.5 mV	19.13 mV/dec	75 h	[121]
Ni_2B/rGO	0.5 M Hydrazine/1.0 M NaOH	Overpotential = 0.3 V	19.13 mV/dec	50 h	[122]
$SNiC_2O_4$-Nb_2O_5/NF	0.5 M Hydrazine/1.0 M KOH	Overpotential = 1.41 V	81 mV/dec	100 h	[127]
NixP/Ni/NF	0.5 M Hydrazine/1.0 M NaOH	Overpotential = 0.3 V	-	100 h	[40]
Mo-Ni_3N/Ni/NF	0.1 M Hydrazine/1.0 M KOH	Overpotential = 0.55 mV	-	110 h	[144]
CoNi-R-S	20 mM Hydrazine /1.0 M KOH	-	67 mV/dec	6,000 s	[142]
Ni SACs/$Ti_3C_2T_x$	0.5 M Hydrazine/1.0 M KOH	Onsetpotential = -0.03 V	62 mV/dec	24,000 s	[153]
PW-Co_3N NWA/NF	0.1 M Hydrazine/1.0 M KOH	Overpotential = 0.358 V	14 mV/dec	10 h	[146]
NiCo@C/MXene/CF	0.5 M Hydrazine/1.0 M KOH	Overpotential = 0.049 V	54.2 mV/dec	125 h	[166]
NiCrO-VcrO nanosheets	0.1M Glycerol/1 M KOH	Overpotential = 1.37 V	13.93 mV/dec	12 h	[175]
β-$Co_{0.1}Ni_{0.9}(OH)_2$	0.05 M EtOH/1 M KOH	Overpotential = 1.29 V	-	20,000 s	[176]
Disordered-β-NiOOH/β-$Ni(OH)_2$	0.004 M HCHO/0.1 M NaOH	Overpotential = 0.4 V	99 mV/dec	-	[178]
NiOOH/Ni_3S_2/NF	0.1 M Glycerol/1 M KOH	Overpotential = 0.073 V	-	24 h	[179]
NiSex/Ni NRAs	0.1 M Glycerol/1 M KOH	Overpotential = 1.43 V	114.73 mV/dec	48 h	[180]
NiS-based electrode	1 M MeOH/1 M KOH 1 M EtOH/1 M KOH	Overpotential = 1.368 V Overpotential = 1.339 V	- -	10,000 s	[181]
Pd-Ni-P	1 M EtOH/0.1 M KOH	Overpotential = 0.11 V	92 mV/dec	120 min	[182]
$PtNi_2$/$Ni(OH)_x$	1 M Glycerol/1 M KOH	Overpotential = 0.8 V	-	2 h	[184]

LDH: Layered double hydroxides; CFC: carbon fiber cloth; SACs: single-atom catalysts; NRAs: nanorod arrays; CF: copper foam.

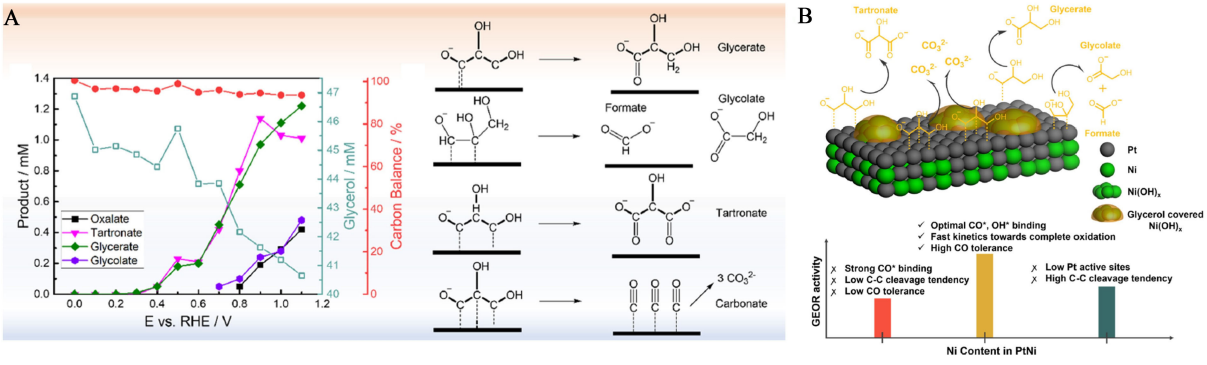

Figure 17. (A) Products formed at different potentials with the Pt/C catalyst detected by online sampling coupled with HPLC. Each potential was held for 10 min, and 200 μL of electrolyte containing glycerol and oxidation products were withdrawn at the end of chronoamperometry. Formate should also be produced during the reaction. However, its HPLC signal is embedded in the glycerol peak and thus cannot be quantified; (B) Illustration of the Electronic Effect in PtNi Electrocatalysts (Green: Ni, gray: Pt) Under Potential less than 1 V (*vs.* RHE)[184]. This figure is quoted with permission from Luo *et al.* HPLC: High-performance liquid chromatography; RHE: reversible hydrogen electrode.

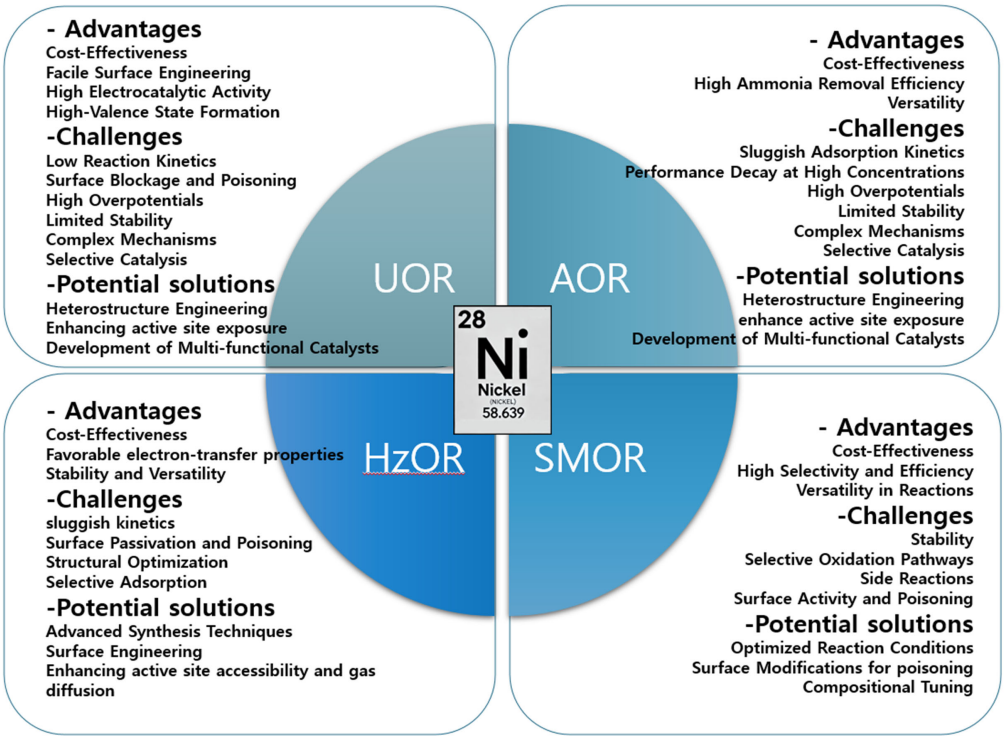

Figure 18. Summary of outlook highlighting the advantages, challenges and potential solutions of Ni-based electrocatalyst for different applications. UOR: Urea oxidation reaction; AOR:ammonia oxidation reaction; HzOR: hydrazine oxidation reaction; SMOR: small molecule oxidation.

In situ spectroscopy, such as High-energy-resolution fluorescence-detected X-ray absorption spectroscopy (HERFD-XAS) and Ambient pressure (AP) XPS, bridges academia and industry by providing precise insights into the electronic and geometric changes of catalysts under operational conditions. HERFD-XAS identifies shifts in oxidation states and coordination environments, while AP-XPS monitors real-time structural transformations, such as $Ni(OH)_2$ converting to active NiOOH species. These techniques offer actionable data on catalyst behavior, crucial for industrial-scale optimization.

In summary, despite challenges, advancements in Ni-based electrocatalysts are driving sustainable hydrogen production. Current research offers a foundation for innovations in catalyst design. Interdisciplinary efforts in materials science, electrochemistry, and modeling can accelerate the development of efficient, durable catalysts, supporting global energy sustainability.

DECLARATIONS

Authors' contributions

Topic selection, literature search, manuscript writing: Kim, M.; Joung, S.
Manuscript discussion and data curation: Kim, M.; Lee, S.; Kwon, H.
Topic selection, manuscript review, editing and supervision: Lee, H.

Availability of data and materials

Not applicable.

Financial support and sponsorship

This work was supported by the National Research Foundation of Korea (NRF) grant (NRF-2022R1A2C2093415), the Korea Basic Science Institute (National Research Facilities and Equipment Center) grant funded by the Ministry of Education (2022R1A6C101A751), and the SungKyunKwan University and the BK21 FOUR (Graduate School Innovation) funded by the Ministry of Education (MOE, Korea) and NRF.

Conflicts of interest

All authors declared that there are no conflicts of interest.

Ethical approval and consent to participate

Not applicable.

Consent for publication

Not applicable.

REFERENCES

1. Welsby, D.; Price, J.; Pye, S.; Ekins, P. Unextractable fossil fuels in a 1.5 °C world. *Nature* **2021**, *597*, 230-4. DOI
2. Zhang, H.; Nai, J.; Yu, L.; Lou, X. W. Metal-organic-framework-based materials as platforms for renewable energy and environmental applications. *Joule* **2017**, *1*, 77-107. DOI
3. Glenk, G.; Reichelstein, S. Economics of converting renewable power to hydrogen. *Nat. Energy.* **2019**, *4*, 216-22. DOI
4. Kazemi, A.; Manteghi, F.; Tehrani, Z. Metal Electrocatalysts for hydrogen production in water splitting. *ACS. Omega.* **2024**, *9*, 7310-35. DOI PubMed PMC
5. Staffell, I.; Scamman, D.; Velazquez, A. A.; et al. The role of hydrogen and fuel cells in the global energy system. *Energy. Environ. Sci.* **2019**, *12*, 463-91. DOI
6. Gunathilake, C.; Soliman, I.; Panthi, D.; et al. A comprehensive review on hydrogen production, storage, and applications. *Chem. Soc. Rev.* **2024**, *53*, 10900-69. DOI
7. Pickering, B.; Lombardi, F.; Pfenninger, S. Diversity of options to eliminate fossil fuels and reach carbon neutrality across the entire European energy system. *Joule* **2022**, *6*, 1253-76. DOI PubMed PMC
8. Parkinson, B.; Balcombe, P.; Speirs, J. F.; Hawkes, A. D.; Hellgardt, K. Levelized cost of CO_2 mitigation from hydrogen production routes. *Energy. Environ. Sci.* **2019**, *12*, 19-40. DOI
9. Wu, W.; Zhai, H.; Holubnyak, E. Technological evolution of large-scale blue hydrogen production toward the U.S. hydrogen energy earthshot. *Nat. Commun.* **2024**, *15*, 5684. DOI PubMed PMC
10. Li, W.; Feaster, J. T.; Akhade, S. A.; et al. Comparative techno-economic and life cycle analysis of water oxidation and hydrogen oxidation at the anode in a CO_2 electrolysis to ethylene system. *ACS. Sustainable. Chem. Eng.* **2021**, *9*, 14678-89. DOI
11. Lu, F.; Zhang, Y.; Liu, S.; et al. Surface proton transfer promotes four-electron oxygen reduction on gold nanocrystal surfaces in alkaline solution. *J. Am. Chem. Soc.* **2017**, *139*, 7310-7. DOI
12. Zegeye, T. A.; Chen, W.; Hsu, C.; Valinton, J. A. A.; Chen, C. Activation energy assessing potential-dependent activities and site reconstruction for oxygen evolution. *ACS. Energy. Lett.* **2022**, *7*, 2236-43. DOI
13. Arshad, F.; Haq, T. U.; Hussain, I.; Sher, F. Recent advances in electrocatalysts toward alcohol-assisted, energy-saving hydrogen production. *ACS. Appl. Energy. Mater.* **2021**, *4*, 8685-701. DOI
14. Guo, W.; Zhang, K.; Liang, Z.; Zou, R.; Xu, Q. Electrochemical nitrogen fixation and utilization: theories, advanced catalyst materials and system design. *Chem. Soc. Rev.* **2019**, *48*, 5658-716. DOI
15. Wang, H.; Sun, M.; Ren, J.; Yuan, Z. Circumventing challenges: design of anodic electrocatalysts for hybrid water electrolysis systems. *Adv. Energy. Mater.* **2023**, *13*, 2203568. DOI
16. Lu, Y.; Chen, M.; Wang, Y.; Yang, C.; Zou, Y.; Wang, S. Aqueous electrocatalytic small-molecule valorization trilogy. *Chem* **2024**, *10*, 1371-90. DOI
17. Boggs, B. K.; King, R. L.; Botte, G. G. Urea electrolysis: direct hydrogen production from urine. *Chem. Commun.* **2009**, 4859-61. DOI PubMed
18. Fukumoto, Y.; Matsunaga, T.; Hayashi, T. Electrocatalytic activities of metal electrodes in anodic oxidation of hydrazine in alkaline solution. *Electrochim. Acta.* **1981**, *26*, 631-6. DOI
19. Yao, K.; Cheng, Y. Investigation of the electrocatalytic activity of nickel for ammonia oxidation. *Mater. Chem. Phys.* **2008**, *108*, 247-

50. DOI
20. Lyu, F.; Wang, Q.; Choi, S. M.; Yin, Y. Noble-metal-free electrocatalysts for oxygen evolution. *Small* **2019**, *15*, 1804201. DOI PubMed
21. Zhang, H.; Gu, H.; Shi, G.; et al. Two-dimensional covalent framework derived nonprecious transition metal single-atomic-site electrocatalyst toward high-efficiency oxygen reduction. *Nano. Lett.* **2023**, *23*, 3803-9. DOI
22. Jiang, K.; Li, J.; Zheng, Z.; et al. Bimetallic phosphide NiCoP electrocatalyst synthesized by one-step electrodeposition for efficient hydrogen evolution in acidic and alkaline solution. *ACS. Appl. Energy. Mater.* **2024**, *7*, 7895-905. DOI
23. Park, G. D.; Park, J.; Kim, J. K.; Kang, Y. C. Recent advances in heterostructured anode materials with multiple anions for advanced alkali-ion batteries. *Adv. Energy. Mater.* **2021**, *11*, 2003058. DOI
24. Ahmad, M. U.; Suresh, G.; Bang, J. H. Rescrutinizing the iron effect on oxygen evolution reaction catalysts under industrially relevant working conditions: overlooked mass transfer limitation driven by the iron incorporation. *ACS. Energy. Lett.* **2024**, *9*, 4953-8. DOI
25. Du, R.; Zhang, N.; Zhu, J.; et al. Nitrogen-doped carbon nanotube aerogels for high-performance ORR catalysts. *Small* **2015**, *11*, 3903-8. DOI
26. Singh, B.; Gawande, M. B.; Kute, A. D.; et al. Single-atom (iron-based) catalysts: synthesis and applications. *Chem. Rev.* **2021**, *121*, 13620-97. DOI
27. Masa, J.; Xia, W.; Muhler, M.; Schuhmann, W. On the role of metals in nitrogen-doped carbon electrocatalysts for oxygen reduction. *Angew. Chem. Int. Ed.* **2015**, *54*, 10102-20. DOI PubMed
28. Gerber, I. C.; Serp, P. A theory/experience description of support effects in carbon-supported catalysts. *Chem. Rev.* **2020**, *120*, 1250-349. DOI PubMed
29. Etesami, M.; Nguyen, M. T.; Yonezawa, T.; Tuantranont, A.; Somwangthanaroj, A.; Kheawhom, S. 3D carbon nanotubes-graphene hybrids for energy conversion and storage applications. *Chem. Eng. J.* **2022**, *446*, 137190. DOI
30. Shah, S. S. A.; Najam, T.; Bashir, M. S.; et al. Identification of catalytic active sites for durable proton exchange membrane fuel cell: catalytic degradation and poisoning perspectives. *Small* **2022**, *18*, 2106279. DOI
31. Barman, B. K.; Sarkar, B.; Ghosh, P.; Ghosh, M.; Mohan, R. G.; Nanda, K. K. In situ decoration of ultrafine Ru nanocrystals on n-doped graphene tube and their applications as oxygen reduction and hydrogen evolution catalyst. *ACS. Appl. Energy. Mater.* **2019**, *2*, 7330-9. DOI
32. Choi, J.; Seo, S.; Kim, M.; Han, Y.; Shao, X.; Lee, H. Relationship between Structure and performance of atomic-scale electrocatalysts for water splitting. *Small* **2024**, *20*, 2304560. DOI
33. Lang, R.; Du, X.; Huang, Y.; et al. Single-atom catalysts based on the metal-oxide interaction. *Chem. Rev.* **2020**, *120*, 11986-2043. DOI
34. Chen, J.; Zhang, Y.; Zhang, Z.; et al. Metal-support interactions for heterogeneous catalysis: mechanisms, characterization techniques and applications. *J. Mater. Chem. A.* **2023**, *11*, 8540-72. DOI
35. Li, R.; Luo, L.; Ma, X.; Wu, W.; Wang, M.; Zeng, J. Single atoms supported on metal oxides for energy catalysis. *J. Mater. Chem. A.* **2022**, *10*, 5717-42. DOI
36. De, S.; Burange, A. S.; Luque, R. Conversion of biomass-derived feedstocks into value-added chemicals over single-atom catalysts. *Green. Chem.* **2022**, *24*, 2267-86. DOI
37. Che, W.; Tao, T.; Baek, J. Strategies for boosting the activity of single-atom catalysts for future energy applications. *J. Mater. Chem. A.* **2022**, *10*, 10297-325. DOI
38. He, T.; Puente-santiago, A. R.; Xia, S.; Ahsan, M. A.; Xu, G.; Luque, R. Experimental and theoretical advances on single atom and atomic cluster-decorated low-dimensional platforms towards superior electrocatalysts. *Adv. Energy. Mater.* **2022**, *12*, 2200493. DOI
39. Zhao, X.; Levell, Z. H.; Yu, S.; Liu, Y. Atomistic understanding of two-dimensional electrocatalysts from first principles. *Chem. Rev.* **2022**, *122*, 10675-709. DOI
40. Liu, J.; Wen, H.; Zhang, Z.; Wang, P. An amorphous/nanocrystalline NixP/Ni heterojunction for electrooxidation of hydrazine. *J. Mater. Chem. A.* **2023**, *11*, 14213-20. DOI
41. Zhang, Y.; Lv, Q.; Chi, K.; et al. Hierarchical porous carbon heterojunction flake arrays derived from metal organic frameworks and ionic liquid for H_2O_2 electrochemical detection in cancer tissue. *Nano. Res.* **2021**, *14*, 1335-43. DOI
42. Gawande, M. B.; Goswami, A.; Asefa, T.; et al. Core-shell nanoparticles: synthesis and applications in catalysis and electrocatalysis. *Chem. Soc. Rev.* **2015**, *44*, 7540-90. DOI
43. Pandikassala, A.; Gangadharan, P. K.; Veedu, R. N.; Kurungot, S. Polydopamine-derived iron-doped hollow carbon nanorods as an efficient bifunctional electrocatalyst for simultaneous generation of hydrogen and electricity. *Energy. Fuels.* **2022**, *36*, 11245-60. DOI
44. Ahsan, M. A.; He, T.; Noveron, J. C.; Reuter, K.; Puente-Santiago, A. R.; Luque, R. Low-dimensional heterostructures for advanced electrocatalysis: an experimental and computational perspective. *Chem. Soc. Rev.* **2022**, *51*, 812-28. DOI PubMed
45. Wang, Z.; Fei, H.; Wu, Y. N. Unveiling advancements: trends and hotspots of metal-organic frameworks in photocatalytic CO_2 reduction. *ChemSusChem* **2024**, *17*, e202400504. DOI
46. Gong, Q.; Yang, D.; Yang, H.; et al. Cobalt ditelluride meets tellurium vacancy: an efficient catalyst as a multifunctional polysulfide mediator toward robust lithium-sulfur batteries. *ACS. Nano.* **2024**, *18*, 28382-93. DOI
47. Moniz, S. J. A.; Shevlin, S. A.; Martin, D. J.; Guo, Z.; Tang, J. Visible-light driven heterojunction photocatalysts for water splitting -

a critical review. *Energy. Environ. Sci.* **2015**, *8*, 731-59. DOI

48. Liu, W.; Xie, J.; Guo, Y.; Lou, S.; Gao, L.; Tang, B. Sulfurization-induced edge amorphization in copper-nickel-cobalt layered double hydroxide nanosheets promoting hydrazine electro-oxidation. *J. Mater. Chem. A.* **2019**, *7*, 24437-44. DOI
49. Huang, C.; Xia, Z.; Wang, J.; et al. Highly efficient and stable electrocatalyst for hydrogen evolution by molybdenum doped Ni-Co phosphide nanoneedles at high current density. *Nano. Res.* **2024**, *17*, 1066-74. DOI
50. Ge, W.; Lin, L.; Wang, S.; et al. Electrocatalytic urea oxidation: advances in mechanistic insights, nanocatalyst design, and applications. *J. Mater. Chem. A.* **2023**, *11*, 15100-21. DOI
51. Gao, X.; Zhang, S.; Wang, P.; Jaroniec, M.; Zheng, Y.; Qiao, S. Z. Urea catalytic oxidation for energy and environmental applications. *Chem. Soc. Rev.* **2024**, *53*, 1552-91. DOI
52. Guo, L.; Zhang, X.; Gan, L.; et al. Advances in selective electrochemical oxidation of 5-hydroxymethylfurfural to produce high-value chemicals. *Adv. Sci.* **2023**, *10*, 2205540. DOI
53. Alzaabi, A.; Almarzooqi, F.; Choi, D. Ammonia electro-catalysis for hydrogen production: Mechanisms, materials, and scalability. *Int. J. Hydrogen. Energy.* **2024**, *94*, 23-52. DOI
54. Liu, H.; Liu, Y.; Li, M.; Liu, X.; Luo, J. Transition-metal-based electrocatalysts for hydrazine-assisted hydrogen production. *Mater. Today. Adv.* **2020**, *7*, 100083. DOI
55. Zheng, X.; Yang, J.; Li, P.; et al. Dual-atom support boosts nickel-catalyzed urea electrooxidation. *Angew. Chem. Int. Ed.* **2023**, *62*, e202217449. DOI
56. Rao, N. N.; Alex, C.; Mukherjee, M.; et al. Evidence for exclusive direct mechanism of urea electro-oxidation driven by *in situ*-generated resilient active species on a rare-earth nickelate. *ACS. Catal.* **2024**, *14*, 981-93. DOI
57. Peng, X.; Zeng, L.; Wang, D.; et al. Electrochemical C-N coupling of CO_2 and nitrogenous small molecules for the electrosynthesis of organonitrogen compounds. *Chem. Soc. Rev.* **2023**, *52*, 2193-237. DOI
58. Wang, T.; Tao, L.; Zhu, X.; et al. Combined anodic and cathodic hydrogen production from aldehyde oxidation and hydrogen evolution reaction. *Nat. Catal.* **2022**, *5*, 66-73. DOI
59. Rollinson, A. N.; Jones, J.; Dupont, V.; Twigg, M. V. Urea as a hydrogen carrier: a perspective on its potential for safe, sustainable and long-term energy supply. *Energy. Environ. Sci.* **2011**, *4*, 1216-24. DOI
60. Rollinson, A. N.; Rickett, G. L.; Lea-langton, A.; Dupont, V.; Twigg, M. V. Hydrogen from urea-water and ammonia-water solutions. *Appl. Catal. B. Environ.* **2011**, *106*, 304-15. DOI
61. Liu, D.; Liu, T.; Zhang, L.; et al. High-performance urea electrolysis towards less energy-intensive electrochemical hydrogen production using a bifunctional catalyst electrode. *J. Mater. Chem. A.* **2017**, *5*, 3208-13. DOI
62. Ding, H.; Zhao, Z.; Zeng, H.; et al. Heterojunction-induced local charge redistribution boosting energy-saving hydrogen production via urea electrolysis. *ACS. Mater. Lett.* **2024**, *6*, 1029-41. DOI
63. Gao, X.; Bai, X.; Wang, P.; et al. Boosting urea electrooxidation on oxyanion-engineered nickel sites via inhibited water oxidation. *Nat. Commun.* **2023**, *14*, 5842. DOI PubMed PMC
64. Ji, Z.; Song, Y.; Zhao, S.; Li, Y.; Liu, J.; Hu, W. Pathway manipulation via Ni, Co, and V ternary synergism to realize high efficiency for urea electrocatalytic oxidation. *ACS. Catal.* **2022**, *12*, 569-79. DOI
65. Wang, Z.; Guo, P.; Liu, M.; et al. Rational design of metallic NiTex (x = 1 or 2) as bifunctional electrocatalysts for efficient urea conversion. *ACS. Appl. Energy. Mater.* **2019**, *2*, 3363-72. DOI
66. Zhou, M.; Weng, Q.; Popov, Z. I.; et al. Construction of polarized carbon-nickel catalytic surfaces for potent, durable, and economic hydrogen evolution reactions. *ACS. Nano.* **2018**, *12*, 4148-55. DOI
67. Fu, X.; Pu, B.; Pan, L.; et al. Composition regulation of Ni-BDC MOF architecture to enhance electrocatalytic urea oxidation in alkaline solution. *Mater. Chem. Front.* **2024**, *8*, 3272-9. DOI
68. Feng, C.; Wang, F.; Liu, Z.; et al. A self-healing catalyst for electrocatalytic and photoelectrochemical oxygen evolution in highly alkaline conditions. *Nat. Commun.* **2021**, *12*, 5980. DOI PubMed PMC
69. Naduvil, K. M. S.; Alex, C.; Rao, N. N.; et al. Unfolding the significance of regenerative active species in nickel hydroxide-based systems for sustained urea electro-oxidation. *Chem. Mater.* **2024**, *36*, 5343-55. DOI
70. Jin, L.; Ji, R.; Wan, H.; et al. Boosting the electrocatalytic urea oxidation performance by amorphous-crystalline Ni-TPA@NiSe heterostructures and mechanism discovery. *ACS. Catal.* **2023**, *13*, 837-47. DOI
71. Zhu, D.; Zhang, H.; Miao, J.; et al. Strategies for designing more efficient electrocatalysts towards the urea oxidation reaction. *J. Mater. Chem. A.* **2022**, *10*, 3296-313. DOI
72. Song, J.; Qian, Z.; Yang, J.; Lin, X.; Xu, Q.; Li, J. In situ/operando investigation for heterogeneous electro-catalysts: from model catalysts to state-of-the-art catalysts. *ACS. Energy. Lett.* **2024**, *9*, 4414-40. DOI
73. Vedharathinam, V.; Botte, G. G. Direct evidence of the mechanism for the electro-oxidation of urea on $Ni(OH)_2$ catalyst in alkaline medium. *Electrochim. Acta.* **2013**, *108*, 660-5. DOI
74. Zhu, X.; Dou, X.; Dai, J.; et al. Metallic nickel hydroxide nanosheets give superior electrocatalytic oxidation of urea for fuel cells. *Angew. Chem. Int. Ed.* **2016**, *55*, 12465-9. DOI
75. Zhao, J.; Zhang, Y.; Guo, H.; et al. Defect-rich $Ni(OH)_2$/NiO regulated by WO_3 as core-shell nanoarrays achieving energy-saving water-to-hydrogen conversion via urea electrolysis. *Chem. Eng. J.* **2022**, *433*, 134497. DOI
76. Huang, C. J.; Xu, H. M.; Shuai, T. Y.; Zhan, Q. N.; Zhang, Z. J.; Li, G. R. Modulation strategies for the preparation of high-performance catalysts for urea oxidation reaction and their applications. *Small* **2023**, *19*, 2301130. DOI PubMed

77. Schranck, A.; Marks, R.; Yates, E.; Doudrick, K. Effect of urine compounds on the electrochemical oxidation of urea using a nickel cobaltite catalyst: an electroanalytical and spectroscopic investigation. *Environ. Sci. Technol.* **2018**, *52*, 8638-48. DOI PubMed
78. Modak, A.; Mohan, R.; Rajavelu, K.; Cahan, R.; Bendikov, T.; Schechter, A. Metal-organic polymer-derived interconnected Fe-Ni alloy by carbon nanotubes as an advanced design of urea oxidation catalysts. *ACS. Appl. Mater. Interfaces.* **2021**, *13*, 8461-73. DOI
79. Vedharathinam, V.; Botte, G. G. Experimental investigation of potential oscillations during the electrocatalytic oxidation of urea on Ni catalyst in alkaline medium. *J. Phys. Chem. C.* **2014**, *118*, 21806-12. DOI
80. Wang, G.; Ling, Y.; Lu, X.; et al. A mechanistic study into the catalytic effect of $Ni(OH)_2$ on hematite for photoelectrochemical water oxidation. *Nanoscale* **2013**, *5*, 4129-33. DOI
81. Liu, G.; Huang, C.; Yang, Z.; Su, J.; Zhang, W. Ultrathin NiMn-LDH nanosheet structured electrocatalyst for enhanced electrocatalytic urea oxidation. *Appl. Catal. A. Gen.* **2021**, *614*, 118049. DOI
82. Tian, T.; Gao, H.; Zhou, X.; et al. Study of the active sites in porous nickel oxide nanosheets by manganese modulation for enhanced oxygen evolution catalysis. *ACS. Energy. Lett.* **2018**, *3*, 2150-8. DOI
83. Rao, R. R.; Corby, S.; Bucci, A.; et al. Spectroelectrochemical analysis of the water oxidation mechanism on doped nickel oxides. *J. Am. Chem. Soc.* **2022**, *144*, 7622-33. DOI PubMed PMC
84. Chia, X.; Pumera, M. Characteristics and performance of two-dimensional materials for electrocatalysis. *Nat. Catal.* **2018**, *1*, 909-21. DOI
85. Feng, D.; Lei, T.; Lukatskaya, M. R.; et al. Robust and conductive two-dimensional metal-organic frameworks with exceptionally high volumetric and areal capacitance. *Nat. Energy.* **2018**, *3*, 30-6. DOI
86. Pu, Y.; Lawrence, M. J.; Celorrio, V.; et al. Nickel confined in 2D earth-abundant oxide layers for highly efficient and durable oxygen evolution catalysts. *J. Mater. Chem. A.* **2020**, *8*, 13340-50. DOI
87. He, X.; Yin, F.; Li, Y.; et al. $NiMnO_3$/$NiMn_2O_4$ oxides synthesized via the aid of pollen: ilmenite/spinel hybrid nanoparticles for highly efficient bifunctional oxygen electrocatalysis. *ACS. Appl. Mater. Interfaces.* **2016**, *8*, 26740-57. DOI
88. Liu, Z.; Zhang, N.; Xiong, Y. In situ raman characterizations for enhanced understandings on electrocatalysis. *J. Phys. Chem. C.* **2024**, *128*, 13651-65. DOI
89. Yang, X.; Zhang, H.; Xu, W.; Yu, B.; Liu, Y.; Wu, Z. A doping element improving the properties of catalysis: *in situ* Raman spectroscopy insights into Mn-doped NiMn layered double hydroxide for the urea oxidation reaction. *Catal. Sci. Technol.* **2022**, *12*, 4471-85. DOI
90. Andaveh, R.; Sabour, R. A.; Seif, A.; et al. In situ assembly of a superaerophobic CoMn/CuNiP heterostructure as a trifunctional electrocatalyst for ampere-level current density urea-assisted hydrogen production. *ACS. Appl. Mater. Interfaces.* **2024**, *16*, 8717-32. DOI
91. Chen, Z.; Wei, W.; Shon, H. K.; Ni, B. Designing bifunctional catalysts for urea electrolysis: progress and perspectives. *Green. Chem.* **2024**, *26*, 631-54. DOI
92. Yan, X.; Hu, Q.; Wang, G.; et al. NiCo layered double hydroxide/hydroxide nanosheet heterostructures for highly efficient electro-oxidation of urea. *Int. J. Hydrogen. Energy.* **2020**, *45*, 19206-13. DOI
93. Miao, F.; Cui, P.; Gu, T.; Yu, S.; Yan, Z.; Hai, G. Dual cation-modified hierarchical nickel hydroxide nanosheet arrays as efficient and robust electrocatalysts for the urea oxidation reaction. *Dalton. Trans.* **2024**, *53*, 1599-606. DOI
94. Periyasamy, S.; Subramanian, P.; Levi, E.; Aurbach, D.; Gedanken, A.; Schechter, A. Exceptionally active and stable spinel nickel manganese oxide electrocatalysts for urea oxidation reaction. *ACS. Appl. Mater. Interfaces.* **2016**, *8*, 12176-85. DOI PubMed
95. Sharma, S.; Kadyan, P.; Sharma, R. K.; Kumar, N.; Grover, S. Progressive updates on nickel hydroxide and its nanocomposite for electrochemical electrode material in asymmetric supercapacitor device. *J. Energy. Storage.* **2024**, *87*, 111368. DOI
96. Ge, J.; Kuang, J.; Xiao, Y.; Guan, M.; Yang, C. Recent development of nickel-based catalysts and in situ characterization techniques for mechanism understanding of the urea oxidation reaction. *Surf. Interfaces.* **2023**, *41*, 103230. DOI
97. Yang, K.; Hao, L.; Hou, Y.; Zhang, J.; Yang, J. Summary and application of Ni-based catalysts for electrocatalytic urea oxidation. *Int. J. Hydrogen. Energy.* **2024**, *51*, 966-81. DOI
98. Jeon, S. S.; Lim, J.; Kang, P. W.; Lee, J. W.; Kang, G.; Lee, H. Design principles of NiFe-layered double hydroxide anode catalysts for anion exchange membrane water electrolyzers. *ACS. Appl. Mater. Interfaces.* **2021**, *13*, 37179-86. DOI
99. Jiang, L.; Pan, Y.; Zhang, J.; et al. Mo propellant boosting the activity of Ni-P for efficient urea-assisted water electrolysis of hydrogen evolution. *J. Colloid. Interface. Sci.* **2022**, *622*, 192-201. DOI
100. Liu, H.; Zhu, S.; Cui, Z.; Li, Z.; Wu, S.; Liang, Y. Ni_2P nanoflakes for the high-performing urea oxidation reaction: linking active sites to a UOR mechanism. *Nanoscale* **2021**, *13*, 1759-69. DOI
101. Yun, W. H.; Das, G.; Kim, B.; Park, B. J.; Yoon, H. H.; Yoon, Y. S. Ni-Fe phosphide deposited carbon felt as free-standing bifunctional catalyst electrode for urea electrolysis. *Sci. Rep.* **2021**, *11*, 22003. DOI PubMed PMC
102. Vij, V.; Sultan, S.; Harzandi, A. M.; et al. Nickel-based electrocatalysts for energy-related applications: oxygen reduction, oxygen evolution, and hydrogen evolution reactions. *ACS. Catal.* **2017**, *7*, 7196-225. DOI
103. Zeng, L.; Liu, Z.; Sun, K.; et al. Multiple modulations of pyrite nickel sulfides *via* metal heteroatom doping engineering for boosting alkaline and neutral hydrogen evolution. *J. Mater. Chem. A.* **2019**, *7*, 25628-40. DOI
104. Guo, X.; Qiu, L.; Li, M.; et al. Accelerating the generation of NiOOH by in-situ surface phosphating nickel sulfide for promoting the proton-coupled electron transfer kinetics of urea electrolysis. *Chem. Eng. J.* **2024**, *483*, 149264. DOI
105. Chang, F.; Gao, W.; Guo, J.; Chen, P. Emerging materials and methods toward ammonia-based energy storage and conversion. *Adv.*

Mater. **2021**, *33*, 2005721. DOI

106. Chen, L.; Shi, J. Chemical-assisted hydrogen electrocatalytic evolution reaction (CAHER). *J. Mater. Chem. A.* **2018**, *6*, 13538-48. DOI
107. Fang, J. Y.; Zheng, Q. Z.; Lou, Y. Y.; et al. Ampere-level current density ammonia electrochemical synthesis using CuCo nanosheets simulating nitrite reductase bifunctional nature. *Nat. Commun.* **2022**, *13*, 7899. DOI PubMed PMC
108. Herron, J. A.; Ferrin, P.; Mavrikakis, M. Electrocatalytic oxidation of ammonia on transition-metal surfaces: a first-principles study. *J. Phys. Chem. C.* **2015**, *119*, 14692-701. DOI
109. Hassan, N. S.; Jalil, A. A.; Saravanan, R.; et al. Recent progress on electrocatalysts in ammonia electrooxidation reaction for clean hydrogen production. *J. Mater. Chem. A.* **2024**, *12*, 23202-17. DOI
110. Pillai, H. S.; Li, Y.; Wang, S. H.; et al. Interpretable design of Ir-free trimetallic electrocatalysts for ammonia oxidation with graph neural networks. *Nat. Commun.* **2023**, *14*, 792. DOI PubMed PMC
111. Zhu, M.; Yang, Y.; Xi, S.; et al. Deciphering NH_3 adsorption kinetics in ternary Ni-Cu-Fe oxyhydroxide toward efficient ammonia oxidation reaction. *Small* **2021**, *17*, 2005616. DOI
112. Samanta, R.; Shekhawat, A.; Sahu, P.; Barman, S. Review and perspective of nickel and its derived catalysts for different electrochemical synthesis reactions in alkaline media for hydrogen production. *Energy. Fuels.* **2024**, *38*, 73-104. DOI
113. Wang, Y.; Ling, Y.; Wang, B.; et al. A review of progress in proton ceramic electrochemical cells: material and structural design, coupled with value-added chemical production. *Energy. Environ. Sci.* **2023**, *16*, 5721-70. DOI
114. Katsounaros, I.; Figueiredo, M. C.; Calle-vallejo, F.; et al. On the mechanism of the electrochemical conversion of ammonia to dinitrogen on Pt(100) in alkaline environment. *J. Catal.* **2018**, *359*, 82-91. DOI
115. Burshtein, T. Y.; Yasman, Y.; Muñoz-moene, L.; Zagal, J. H.; Eisenberg, D. Hydrazine oxidation electrocatalysis. *ACS. Catal.* **2024**, *14*, 2264-83. DOI
116. Tong, Y.; Chen, P. Recent progress of advanced electrocatalysts for hydrogen production *via* hydrazine-assisted water electrolysis. *Inorg. Chem. Front.* **2024**, *11*, 6218-45. DOI
117. Matsumoto, M.; Kano, H.; Suzuki, M.; Katagiri, T.; Umeda, Y.; Fukushima, S. Carcinogenicity and chronic toxicity of hydrazine monohydrate in rats and mice by two-year drinking water treatment. *Regul. Toxicol. Pharmacol.* **2016**, *76*, 63-73. DOI PubMed
118. Zhu, W.; Gandi, N. A.; Wu, Q.; et al. Simultaneous electrocatalytic hydrogen production and hydrazine removal from acidic waste water. *Chem. Eng. Sci.* **2022**, *258*, 117769. DOI
119. Attia, A. A.; Silaghi-Dumitrescu, R. Computational investigation of the initial two-electron, two-proton steps in the reaction mechanism of hydroxylamine oxidoreductase. *J. Phys. Chem. B.* **2014**, *118*, 12140-5. DOI PubMed
120. Zhou, H.; Xiong, B.; Chen, L.; Shi, J. Modulation strategies of Cu-based electrocatalysts for efficient nitrogen reduction. *J. Mater. Chem. A.* **2020**, *8*, 20286-93. DOI
121. Wang, Z.; Xu, L.; Huang, F.; et al. Copper-nickel nitride nanosheets as efficient bifunctional catalysts for hydrazine-assisted electrolytic hydrogen production. *Adv. Energy. Mater.* **2019**, *9*, 1900390. DOI
122. Wen, H.; Chen, C.; Tang, P.; Wang, P. Ultrasmall nickel boride nanoparticles supported on reduced graphene oxide as a high-performance catalyst for hydrazine electrooxidation. *Electrochim. Acta.* **2023**, *471*, 143364. DOI
123. Sakamoto, T.; Masuda, T.; Yoshimoto, K.; et al. NiO/Nb_2O_5/C hydrazine electrooxidation catalysts for anion exchange membrane fuel cells. *J. Electrochem. Soc.* **2017**, *164*, F229-34. DOI
124. Uddin, M. E.; Kim, N. H.; Kuila, T.; Lee, S. H.; Hui, D.; Lee, J. H. Preparation of reduced graphene oxide-$NiFe_2O_4$ nanocomposites for the electrocatalytic oxidation of hydrazine. *Compos. Part. B. Eng.* **2015**, *79*, 649-59. DOI
125. Askari, M. B.; Salarizadeh, P.; Beitollahi, H.; Tajik, S.; Eshghi, A.; Azizi, S. Electro-oxidation of hydrazine on $NiFe_2O_4$-rGO as a high-performance nano-electrocatalyst in alkaline media. *Mater. Chem. Phys.* **2022**, *275*, 125313. DOI
126. Yang, X.; Bu, H.; Qi, R.; et al. Boosting urea-assisted water splitting over P-MoO_2@CoNiP through Mo leaching/reabsorption coupling CoNiP reconstruction. *J. Colloid. Interface. Sci.* **2024**, *676*, 445-58. DOI
127. Chen, X. H.; Fu, H. C.; Wu, L. L.; et al. Tuning the d-band center of NiC_2O_4 with Nb_2O_5 to optimize the Volmer step for hydrazine oxidation-assisted hydrogen production. *Green. Chem.* **2022**, *24*, 5559-69. DOI
128. Rathore, D.; Banerjee, A.; Pande, S. Bifunctional tungsten-Doped $Ni(OH)_2$/NiOOH nanosheets for overall water splitting in an alkaline medium. *ACS. Appl. Nano. Mater.* **2022**, *5*, 2664-77. DOI
129. Ren, J.; Chen, L.; Wang, H.; Tian, W.; Yuan, Z. Water electrolysis for hydrogen production: from hybrid systems to self-powered/catalyzed devices. *Energy. Environ. Sci.* **2024**, *17*, 49-113. DOI
130. Fan, G.; Li, F.; Evans, D. G.; Duan, X. Catalytic applications of layered double hydroxides: recent advances and perspectives. *Chem. Soc. Rev.* **2014**, *43*, 7040-66. DOI PubMed
131. Babar, P.; Lokhande, A.; Karade, V.; et al. Trifunctional layered electrodeposited nickel iron hydroxide electrocatalyst with enhanced performance towards the oxidation of water, urea and hydrazine. *J. Colloid. Interface. Sci.* **2019**, *557*, 10-7. DOI
132. Parra-puerto, A.; Ng, K. L.; Fahy, K.; Goode, A. E.; Ryan, M. P.; Kucernak, A. Supported transition metal phosphides: activity survey for HER, ORR, OER, and corrosion resistance in acid and alkaline electrolytes. *ACS. Catal.* **2019**, *9*, 11515-29. DOI
133. Blanchard, P. E. R.; Grosvenor, A. P.; Cavell, R. G.; Mar, A. X-ray photoelectron and absorption spectroscopy of metal-rich phosphides M_2P and M_3P (M = Cr-Ni). *Chem. Mater.* **2008**, *20*, 7081-8. DOI
134. Zhu, Y.; Lu, P.; Li, F.; Ding, Y.; Chen, Y. Metal-rich porous copper cobalt phosphide nanoplates as a high-rate and stable battery-type cathode material for battery-supercapacitor hybrid devices. *ACS. Appl. Energy. Mater.* **2021**, *4*, 3962-74. DOI

135. Zhu, L.; Huang, J.; Meng, G.; et al. Active site recovery and N-N bond breakage during hydrazine oxidation boosting the electrochemical hydrogen production. *Nat. Commun.* **2023**, *14*, 1997. DOI PubMed PMC
136. Li, S. H.; Qi, M. Y.; Tang, Z. R.; Xu, Y. J. Nanostructured metal phosphides: from controllable synthesis to sustainable catalysis. *Chem. Soc. Rev.* **2021**, *50*, 7539-86. DOI PubMed
137. Li, C.; Wang, Y.; Wang, X.; Azam, T.; Wu, Z. Electrochemical refining of energy-saving coupled systems toward generation of high-value chemicals. *Chem* **2024**, *10*, 2666-99. DOI
138. Behera, S.; Ganguly, S.; Loha, C.; Mondal, B.; Ghosh, S. Critical role of interface design in acceleration of overall water splitting and hybrid electrolysis process: state of the art and perspectives. *Energy. Fuels.* **2023**, *37*, 7603-33. DOI
139. Zhai, P.; Zhang, Y.; Wu, Y.; et al. Engineering active sites on hierarchical transition bimetal oxides/sulfides heterostructure array enabling robust overall water splitting. *Nat. Commun.* **2020**, *11*, 5462. DOI PubMed PMC
140. Yang, C.; Wang, T.; Li, C.; Li, Y.; Liu, D.; Zhang, Q. Recent progress on 2D material-based nanoarchitectures for small molecule electro-oxidation. *Mater. Chem. Front.* **2024**, *8*, 404-33. DOI
141. Zhou, L.; Shao, M.; Zhang, C.; et al. Hierarchical CoNi-sulfide nanosheet arrays derived from layered double hydroxides toward efficient hydrazine electrooxidation. *Adv. Mater.* **2017**, 29. DOI
142. Moges, E. A.; Chang, C.; Tsai, M.; Su, W.; Hwang, B. J. Electrocatalysts for value-added electrolysis coupled with hydrogen evolution. *EES. Catal.* **2023**, *1*, 413-33. DOI
143. Wu, Y.; Liu, X.; Han, D.; et al. Electron density modulation of $NiCo_2S_4$ nanowires by nitrogen incorporation for highly efficient hydrogen evolution catalysis. *Nat. Commun.* **2018**, *9*, 1425. DOI PubMed PMC
144. Liu, Y.; Zhang, J.; Li, Y.; Qian, Q.; Li, Z.; Zhang, G. Realizing the synergy of interface engineering and chemical substitution for Ni_3N enables its bifunctionality toward hydrazine oxidation assisted energy-saving hydrogen production. *Adv. Funct. Mater.* **2021**, *31*, 2103673. DOI
145. Li, K.; Zhou, G.; Tong, Y.; Ye, Y.; Chen, P. Interface engineering of a hierarchical p-modified Co/Ni_3P heterostructure for highly efficient water electrolysis coupled with hydrazine degradation. *ACS. Sustainable. Chem. Eng.* **2023**, *11*, 14186-96. DOI
146. Wang, X.; Hu, H.; Yan, X.; Zhang, Z.; Yang, M. Activating interfacial electron redistribution in lattice-matched biphasic Ni_3N-Co_3N for energy-efficient electrocatalytic hydrogen production via coupled hydrazine degradation. *Angew. Chem. Int. Ed.* **2024**, *63*, e202401364. DOI
147. Dou, J.; Sun, Z.; Opalade, A. A.; Wang, N.; Fu, W.; Tao, F. F. Operando chemistry of catalyst surfaces during catalysis. *Chem. Soc. Rev.* **2017**, *46*, 2001-27. DOI
148. Xu, Q.; Zhang, J.; Zhang, H.; et al. Atomic heterointerface engineering overcomes the activity limitation of electrocatalysts and promises highly-efficient alkaline water splitting. *Energy. Environ. Sci.* **2021**, *14*, 5228-59. DOI
149. Su, J.; Zhang, S.; Liu, Q.; Hu, G.; Zhang, L. The janus in monodispersed catalysts: synergetic interactions. *J. Mater. Chem. A.* **2021**, *9*, 5276-95. DOI
150. Chen, Y.; Ji, S.; Chen, C.; Peng, Q.; Wang, D.; Li, Y. Single-atom catalysts: synthetic strategies and electrochemical applications. *Joule* **2018**, *2*, 1242-64. DOI
151. Wang, Y.; Su, H.; He, Y.; et al. Advanced electrocatalysts with single-metal-atom active sites. *Chem. Rev.* **2020**, *120*, 12217-314. DOI
152. Huang, C.; Dong, J.; Sun, W.; et al. Coordination mode engineering in stacked-nanosheet metal-organic frameworks to enhance catalytic reactivity and structural robustness. *Nat. Commun.* **2019**, *10*, 2779. DOI
153. Zhou, S.; Zhao, Y.; Shi, R.; et al. Vacancy-rich MXene-immobilized Ni single atoms as a high-performance electrocatalyst for the hydrazine oxidation reaction. *Adv. Mater.* **2022**, *34*, 2204388. DOI
154. Liu, Y.; Zhang, J.; Li, Y.; et al. Manipulating dehydrogenation kinetics through dual-doping Co_3N electrode enables highly efficient hydrazine oxidation assisting self-powered H_2 production. *Nat. Commun.* **2020**, *11*, 1853. DOI PubMed PMC
155. Khalafallah, D.; Zhi, M.; Hong, Z. Development trends on nickel-based electrocatalysts for direct hydrazine fuel cells. *ChemCatChem* **2021**, *13*, 81-110. DOI
156. Senthil, R. A.; Jung, S.; Min, A.; et al. Revealing the impact of pulsed laser-produced single-Pd nanoparticles on a bimetallic $NiCo_2O_4$ electrocatalyst for energy-saving hydrogen production via hybrid water electrolysis. *ACS. Catal.* **2024**, *14*, 3320-35. DOI
157. Shih, Y.; Wu, Z.; Luo, J. Electrochemical ammonia oxidation on terephthalic acid framework ($BDC\text{-}NH_2$) derived core-shell nickel oxide/nickel-enriched 2D carbon nanoflakes (NiO/Ni/CNF). *Appl. Catal. B. Environ. Energy.* **2024**, *357*, 124244. DOI
158. Liao, W.; Zhao, Q.; Wang, S.; et al. Insights into mechanisms on electrochemical oxygen evolution substitution reactions. *J. Catal.* **2023**, *428*, 115161. DOI
159. Zhai, Y.; Jin, C.; Xia, Q.; et al. Atomically confined Ru sites in octahedral Co_3O_4 for high-efficiency hydrazine oxidation. *Adv. Funct. Mater.* **2024**, *34*, 2311063. DOI
160. Liu, G.; Nie, T.; Wang, H.; et al. Size sensitivity of supported palladium species on layered double hydroxides for the electro-oxidation dehydrogenation of hydrazine: from nanoparticles to nanoclusters and single atoms. *ACS. Catal.* **2022**, *12*, 10711-7. DOI
161. Xu, X.; Chen, H. C.; Li, L.; et al. Leveraging metal nodes in metal-organic frameworks for advanced anodic hydrazine oxidation assisted seawater splitting. *ACS. Nano.* **2023**, *17*, 10906-17. DOI
162. Hu, Y.; Chao, T.; Li, Y.; et al. Cooperative Ni(Co)-Ru-P sites activate dehydrogenation for hydrazine oxidation assisting self-powered H_2 production. *Angew. Chem. Int. Ed.* **2023**, *62*, e202308800. DOI
163. De, S.; Zhang, J.; Luque, R.; Yan, N. Ni-based bimetallic heterogeneous catalysts for energy and environmental applications. *Energy.*

Environ. Sci. **2016**, *9*, 3314-47. DOI

164. Nakaya, Y.; Furukawa, S. Catalysis of alloys: classification, principles, and design for a variety of materials and reactions. *Chem. Rev.* **2023**, *123*, 5859-947. DOI PubMed
165. Nørskov, J. K.; Bligaard, T.; Hvolbaek, B.; Abild-Pedersen, F.; Chorkendorff, I.; Christensen, C. H. The nature of the active site in heterogeneous metal catalysis. *Chem. Soc. Rev.* **2008**, *37*, 2163-71. DOI PubMed
166. Sun, F.; Qin, J.; Wang, Z.; et al. Energy-saving hydrogen production by chlorine-free hybrid seawater splitting coupling hydrazine degradation. *Nat. Commun.* **2021**, *12*, 4182. DOI PubMed PMC
167. Feng, G.; Kuang, Y.; Li, P.; et al. Single crystalline ultrathin nickel-cobalt alloy nanosheets array for direct hydrazine fuel cells. *Adv. Sci.* **2017**, *4*, 1600179. DOI
168. Sun, Q.; Wang, L.; Shen, Y.; et al. Bifunctional copper-doped nickel catalysts enable energy-efficient hydrogen production via hydrazine oxidation and hydrogen evolution reduction. *ACS. Sustainable. Chem. Eng.* **2018**, *6*, 12746-54. DOI
169. Zhang, Z.; Tang, P.; Wen, H.; Wang, P. Bicontinuous nanoporous Ni-Fe alloy as a highly active catalyst for hydrazine electrooxidation. *J. Alloys. Compd.* **2022**, *906*, 164370. DOI
170. Prajapati, A.; Govindarajan, N.; Sun, W.; et al. Mechanistic insights into the electrochemical oxidation of 5-hydroxymethylfurfural on a thin-film Ni anode. *ACS. Catal.* **2024**, *14*, 10122-31. DOI
171. Li, Z.; Han, Y.; Huang, B.; Xie, Z.; Wei, Q. Electrochemical oxidation of 5-hydroxymethylfurfural over a molybdenum sulfide modified nickel-based catalyst. *Mater. Adv.* **2023**, *4*, 2449-56. DOI
172. Gupta, D.; Kafle, A.; Nagaiah, T. C. Dinitrogen reduction coupled with methanol oxidation for low overpotential electrochemical NH_3 synthesis over cobalt pyrophosphate as bifunctional catalyst. *Small* **2023**, *19*, 2208272. DOI PubMed
173. Simões, M.; Baranton, S.; Coutanceau, C. Electrochemical valorisation of glycerol. *ChemSusChem* **2012**, *5*, 2106-24. DOI PubMed
174. Tuleushova, N.; Holade, Y.; Cornu, D.; Tingry, S. Glycerol electro-reforming in alkaline electrolysis cells for the simultaneous production of value-added chemicals and pure hydrogen - mini-review. *Electrochem. Sci. Adv.* **2023**, *3*, e2100174. DOI
175. Xia, Z.; Ma, C.; Fan, Y.; et al. Vacancy optimized coordination on nickel oxide for selective electrocatalytic oxidation of glycerol. *ACS. Catal.* **2024**, *14*, 1930-8. DOI
176. Chen, W.; Xie, C.; Wang, Y.; et al. Activity origins and design principles of nickel-based catalysts for nucleophile electrooxidation. *Chem* **2020**, *6*, 2974-93. DOI
177. Huang, W.; Ma, X. Y.; Wang, H.; et al. Promoting effect of $Ni(OH)_2$ on palladium nanocrystals leads to greatly improved operation durability for electrocatalytic ethanol oxidation in alkaline solution. *Adv. Mater.* **2017**, 29. DOI
178. Trafela, Š.; Zavašnik, J.; Šturm, S.; Žužek, R. K. Controllable voltammetric formation of a structurally disordered NiOOH/$Ni(OH)_2$ redox pair on Ni-nanowire electrodes for enhanced electrocatalytic formaldehyde oxidation. *Electrochim. Acta.* **2020**, *362*, 137180. DOI
179. Xu, L.; Yang, Y.; Li, C.; et al. Unveiling the mechanism of electrocatalytic oxidation of glycerol by in-situ electrochemical spectroscopy. *Chem. Eng. J.* **2024**, *481*, 148304. DOI
180. Wang, S.; Yan, Y.; Du, Y.; et al. Inhibiting the deep reconstruction of Ni-based interface by coordination of chalcogen anions for efficient and stable glycerol electrooxidation. *Adv. Funct. Mater.* **2024**, *34*, 2404290. DOI
181. Li, J.; Tian, X.; Wang, X.; et al. Electrochemical Conversion of alcohols into acidic commodities on nickel sulfide nanoparticles. *Inorg. Chem.* **2022**, *61*, 13433-41. DOI
182. Jiang, R.; Tran, D. T.; Mcclure, J. P.; Chu, D. A class of (Pd-Ni-P) electrocatalysts for the ethanol oxidation reaction in alkaline media. *ACS. Catal.* **2014**, *4*, 2577-86. DOI
183. Araujo, R. B.; Martín-yerga, D.; Santos, E. C. D.; Cornell, A.; Pettersson, L. G. Elucidating the role of Ni to enhance the methanol oxidation reaction on Pd electrocatalysts. *Electrochim. Acta.* **2020**, *360*, 136954. DOI
184. Luo, H.; Yukuhiro, V. Y.; Fernández, P. S.; et al. Role of Ni in PtNi bimetallic electrocatalysts for hydrogen and value-added chemicals coproduction via glycerol electrooxidation. *ACS. Catal.* **2022**, *12*, 14492-506. DOI
185. Nitaya, T.; Cheng, Y.; Lu, S.; Poochinda, K.; Pruksathorn, K.; Jiang, S. P. Unusual synergetic effect of nickel single atoms on the electrocatalytic activity of palladium for alcohol oxidation reactions in alkaline media. *Chem. Commun.* **2018**, *54*, 12404-7. DOI